Hybrid molybdenum-tungsten oxide as novel plasmonic electrochromic nanomaterial

Auteur : Gillissen, Florian
Promoteur(s) : Cloots, Rudi
Faculté : Faculté des Sciences
Diplôme : Master en sciences chimiques, à finalité spécialisée
Année académique : 2018-2019
URI/URL : http://hdl.handle.net/2268.2/6970

FACULTY OF SCIENCES
Chemistry Department

Group of Research in Energy and ENvironment from MATerials (GREENMAT) – Prof. R. Cloots

Hybrid molybdenum-tungsten oxide as novel plasmonic electrochromic nanomaterial

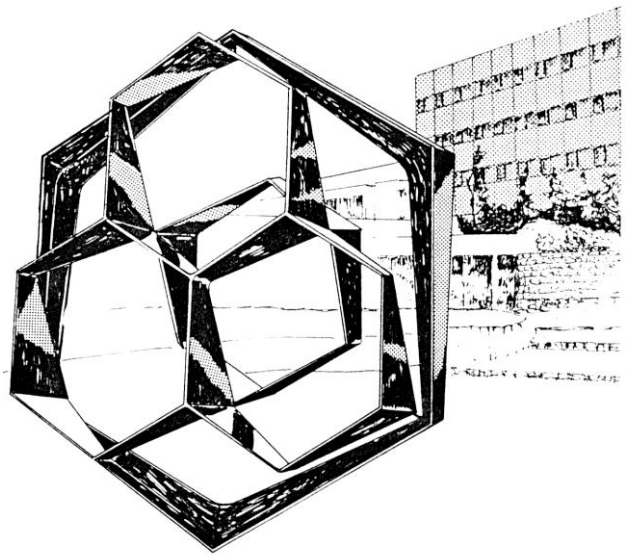

Academic year 2018-2019

Dissertation presented by
Florian Gillissen
for the aquisition of the degree
of Master in Chemical Sciences

Remerciements

Avant tout je tiens à remercier le Professeur Rudi Cloots, qui m'a accueilli au sein du GREENMAT et m'a permis d'y réaliser ce mémoire.

Je remercie également mes encadrants, les Docteurs Anthony Maho et Laura Manceriu, qui m'ont accompagné durant toute la durée de ce travail, pour leur disponibilité, leurs précieux conseils et la confiance qu'ils m'ont accordé tout au long de la réalisation de ce travail ainsi que le temps qu'ils ont dédié aux relectures et corrections de ce manuscrit.

Je voudrais aussi remercier toute l'équipe du GREENMAT, pour leur accueil chaleureux, leur aide généreuse et leur bonne humeur. Merci de nous avoir considérés, mes co-mémorants et moi-même, comme des membres à part entière du laboratoire dès notre arrivée.

Je tiens spécialement à remercier le Docteur Aline Rougier de l'Université de Bordeaux et Issam Mjejri, son post-doctorant, pour les dépôts et les mesures électrochimiques qu'ils ont effectués lors d'une collaboration entre nos universités. Ces résultats ont permis l'aboutissement de ce mémoire et sont très encourageants pour la suite du projet.

Merci aussi à Nicolas Thelen, qui a pris le temps de nous accueillir au CHU et qui s'est occupé pour nous d'obtenir des images TEM de nos échantillons quand nous en avions besoin.

Enfin, je tiens à remercier mes co-mémorants et plus généralement tous les étudiants de Master 2 et Master 1 avec qui j'ai vécu 5 années incroyables, et dont je garderai des souvenirs encore longtemps.

Finalement, je voudrais remercier ma famille et ma petite amie, qui m'ont toujours soutenu dans mes études

Table of content

Chapter 1 – Introduction

1.1. Energy efficiency in buildings and "smart glazing" in energy-efficient buildings

Modern residential and commercial buildings are responsible for nearly 40 % of the total annual energy demand in Europe[1-3]. From these 40 %, heating, ventilation and air conditioning (HVAC) and lighting account for almost two thirds of the consumption[2,4] (*Figure 1*).

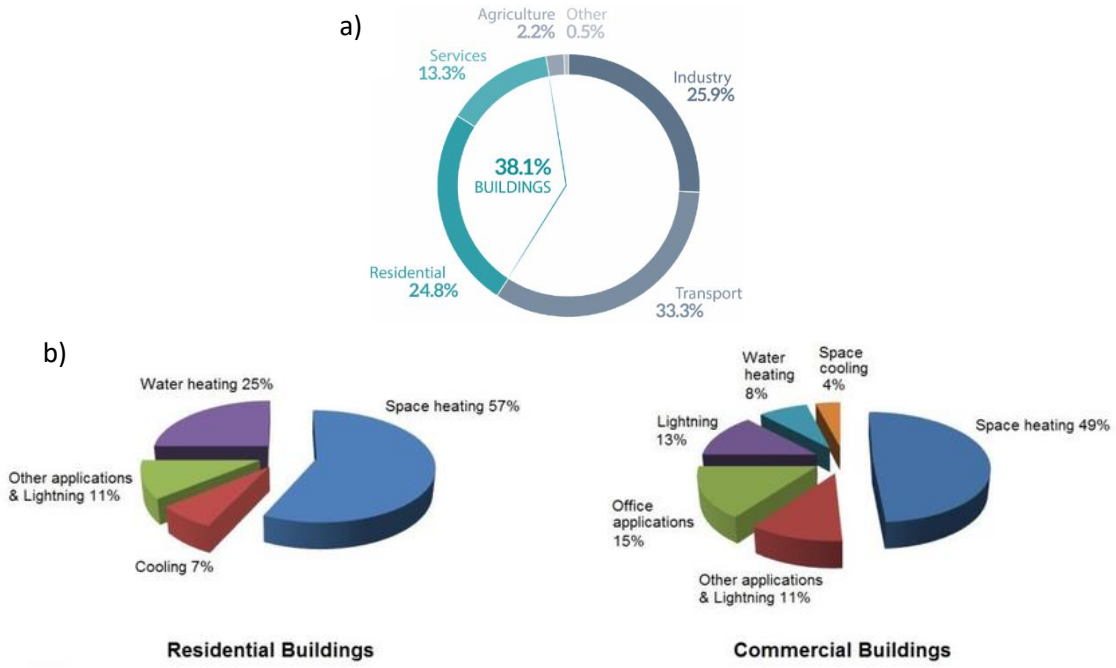

Figure 1: Pie chart of a) the energy demand per sector in Europe[5] and b) the distribution of the consumption in residential (left) and commercial (right) buildings in Europe[4].

Given the current economic and environmental context, energy savings are one of the main concerns society has to deal with. Energy-saving technologies are already well implanted in developed countries, with buildings equipped with solar panels[1], advanced insulation[1], green roofs[6] (among others) in an attempt to minimize the energy demand. However, in most buildings and skyscrapers equipped with very large bay windows, most of the energy is wasted due to the low-efficient fenestration technologies used and the inadaptability to dynamically adapt to changing weather[3].

In this purpose, several technologies have been developed in an attempt to significantly decrease the energy needs and costs. Nowadays, the most widespread ones are multi-paned (double and triple) windows[3], low-emissivity coatings[3,7] and chromogenic materials, especially photo- and thermochromic thin films[3].

While low emissivity (low-E) coatings and multi-paned glazed windows (*Figure 2.a and b*) can selectively modulate the infrared range of the solar radiations[1,7], responsible for most of the heat transfers, while offering high visible transparency, their passive, non-modulable

character represents a major drawback in terms of energy efficiency. Indeed, these technologies lack the possibility of being turned on and off to meet the different requirements of a changing weather depending on the geographical location, the season as well as the varying meteorological conditions throughout the day. Therefore, these technologies cannot dynamically adapt for an optimal management of the energetic demand throughout the whole year and all over the world.

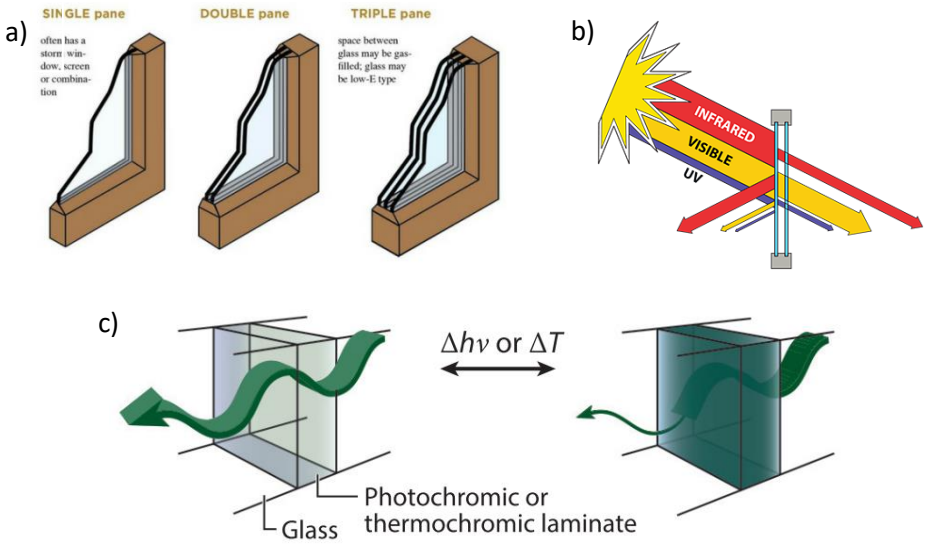

Figure 2: Schematic representation of modern energy-efficient fenestration technologies: a) multi-paned glass windows[8], b) low emissivity coatings[9], c) photo- and thermochromic films[3].

On the other hand, photo- and thermochromic coatings (*Figure 2.c)* are active technologies, meaning they can be triggered by the application of a stimulus, respectively light or heat[3]. This stimulus is responsible for the modification of the optical properties of the active material in the coating, allowing for the partial absorption and/or reflection of the solar radiation over a given wavelength range[3]. However, these dynamically-modulated coating technologies offer no control over the stimulus required to switch the optical properties and therefore often fail to fully meet the user's specific requirements.

The efficient, dynamic and "on demand" modulation of the solar radiations would be of great interest both from an economical and environmental point of view. "Smart windows", capable of dynamically modulating light and heat at the same time, have already been shown to efficiently reduce energy demand up to 40% in comparison to simple passive windows[3]. This technology has already been developed by several industrial actors (SageGlass – Saint Gobain, AGC Glass (Halio™) View…) in order to produce energy-efficient fenestration devices able to dynamically switch between colored and transparent states as well as intermediate state on demand (*Figure 3*). Such glazing technology represents a great opportunity for industrial investments with more than 37 million square meters of windows installed worldwide every year[3].

Figure 3: SageGlass® electrochromic windows, displaying a dynamic modulation of incoming light depending on the applied bias[10].

The requirements for the production of such a device are met by electrochromic coatings, making them the best candidates for the fabrication of an active, dynamic device able to rapidly adapt to changing weather and user's preferences[3].

1.2. Electrochromism and conventional electrochromic materials

a) Materials overview

Selected materials can exhibit what is known as electrochromism, a phenomenon characterized by a modification in their optical properties upon the application of a potential[3,11]. By comparison with similar chromogenic technologies such as photo- and thermochromic coatings, the stimulus required to activate electrochromic materials is easily controllable and can be tuned to dynamically modulate the amount of light transmitted through the device. The application of a bias will cause the active material to reversibly switch between a high transmission state (depicted as "clear" or "bleached" state) and a low transmission state (depicted as "dark" or "colored" state)[3,12] (*Figure 4*). The intensity of the coloration in the dark state depends on the amplitude of the bias and the duration during which it is applied.

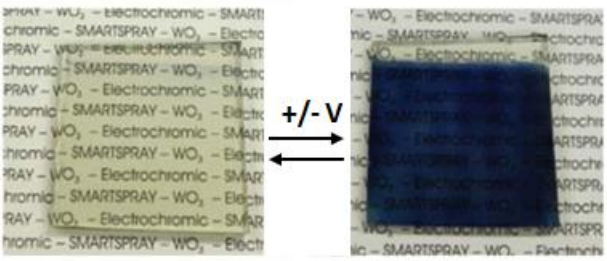

Figure 4: Example of an electrochromic material (based on tungsten oxide WO_3) in the bleached (left) and colored states (right) (SMARTSPRAY®, ULiège-INISMA-UNamur) [11].

Electrochromic properties have been shown in a large array of materials, notably:

- Inorganic metal oxides such as WO_3, NiO, V_2O_5;
- Metallic complexes such as Prussian blue;
- Organic compounds such as viologens;
- Conjugated conductive polymers such as polythiophenes, polypyrroles[3,12].

However, small inorganic particles, organic compounds and polymeric species generally suffer from poor photochemical and electrochemical durability. Their relative instability when exposed to UV radiation and the lack of efficient optical modulation resulting from irreversible redox mechanisms and side reactions can lead to a decrease in efficiency and some undesirable tinting (often yellowish) of the active material over time. Moreover, these materials usually exhibit poor modulation ability over the NIR range[3].

Due to the superior stability shown by inorganic metal oxides[3], only these will be considered for this work. In addition, the high level of control on the thermal behavior of these materials offers a wide array of methods available for their synthesis and deposition. In addition, these compounds are part of the expertise of Prof. Rudi Cloots and of GREENMAT laboratory, who are hosting and supervising this work.

Materials like W, Mo, V, Ir and Ni oxides show the most intense contrast between their colored and bleached states and are thus some of the most studied materials in the electrochromic field[12]. Because of its exceptional properties, namely its long term stability (lifespan extending up to 100k coloration/decoloration cycles), high optical contrast between states (up to 98% contrast in the visible range) and high coloration efficiency (CE)*, WO_3 has drawn most of the attention over the years and anchored itself as the most widely implemented active compound in electrochromic devices[13]. Another widely studied metal oxide is NiO which exhibits good cycling reversibility, a brownish colored state and high ranges of coloration efficiency[14,15]. Anodically-colorable NiO is regularly used as complementary counter-electrode material because of its ability to optically switch in good complementarity with cathodically-colorable WO_3[14,15], leading to an enhanced contrast provided in the device as the coloration of both materials add up in the colored state[12]. NiO has been reported to be stable up to 100k charging cycles and displays maximum CE values of 100 $cm^2\ C^{-1}$ [16].

b) *Principles and mechanisms*

In conventional electrochromic metal oxides, either WO_3 or NiO as representative cases here, the proposed model to explain the modification of optical properties relies on ions electrons pairs either being inserted or extracted into/from the host lattice of the material[3,12,17].

Although other models have been proposed, the most widely accepted one is the intervalence/small polaron model[17]. It describes a localized electronic transition between two neighboring metal centers of different oxidation levels upon the absorption of a photon.

*The coloration efficiency (CE) is defined as[16,20] : $CE = \Delta OD/(Q/S) = (1/(Q/S))\ log(T_{ble}/T_{col})$

With Q the charge density and T_{col} and T_{ble} the transmittance in the colored and bleached states respectively.

When a potential is applied, a fraction of the original material can be oxidized/reduced from the extraction/insertion of electrons. As a consequence, sites with differing oxidation states are created, from which the absorption can arise. When an ion is inserted into the lattice to compensate the insertion of an electron and keep the charge neutrality, the crystalline structure is deformed and the symmetry is locally disrupted. This lattice deformation is accompanied by a corresponding energy which, if it is higher than the energy required for electron hopping, confines the electron in a highly localized trapped state (*Figure 5.a*). The absorption of a photon then brings enough energy to the system for the electron to be transferred from its trapped state to an adjacent metal center with a different oxidation level. Depending on the photon energy required for the transition to take place, an absorption peak will appear in the spectrum of the material at the corresponding wavelength[17] (*Figure 5.b*).

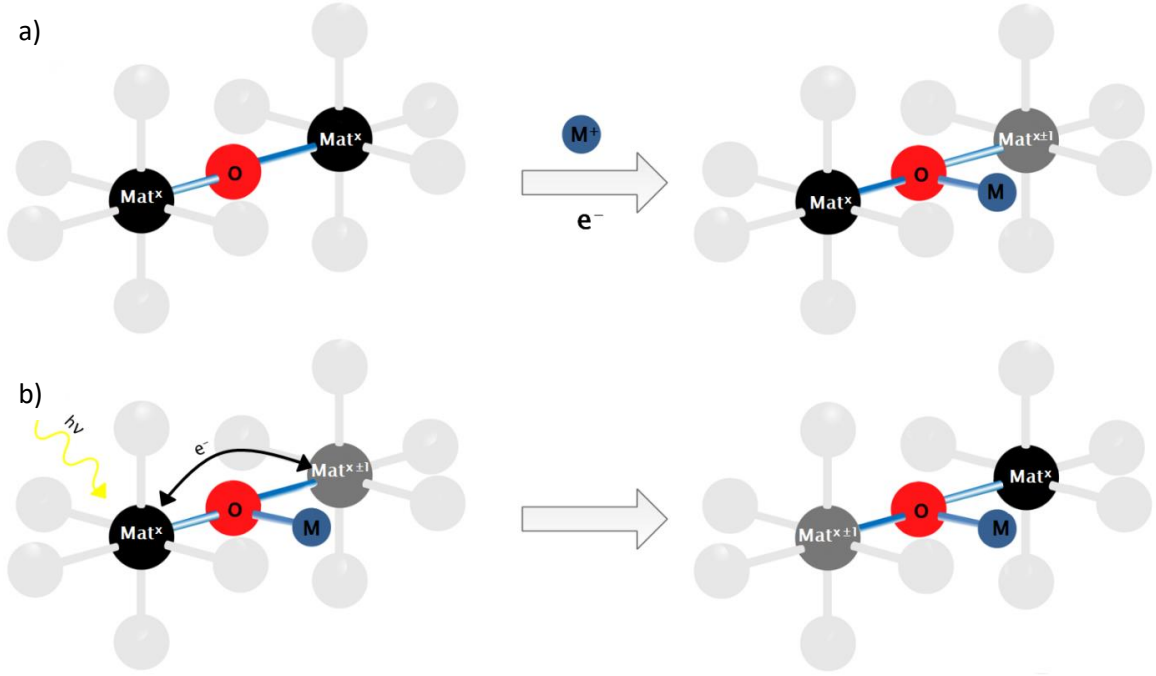

Figure 5: Polaronic absorption mechanism in conventional electrochromic materials: a) reduction/oxidation of a metallic center by the insertion/extraction of charge pairs, b) schematic representation of the absorption of a photon and the resulting electron transfer, responsible for the absorbance of the material[17].

Since this absorption mechanism can arise from both oxidation and reduction of the active material, two types of electrochromic compounds can be defined. On one hand, cathodic electrochromic materials such as WO_3 become colored upon reduction (typically of W^{6+} into W^{5+}) and the compensative insertion of positive ions M^+ such as protons H^+ or Li^+ (and other) alkali ions[3] as shown in *Equation 1* below:

$$Mat\ (transparent) + xM+ + xe^- \rightarrow M_xMat\ (colored) \qquad (1)$$

On the other hand, materials coloring upon oxidation (extraction of electrons and compensative ions from the host lattice, like in NiO and IrO_2 for example) are known as anodically-charged materials[3] (*Equation 2*):

$$M_xMat\ (transparent) \rightarrow Mat\ (colored) + xM+ + xe^- \qquad (2)$$

From the two equations presented above, it can be deduced that cathodic and anodic materials work complementarily, one releasing the ion/electron pairs required for the other one to switch states. Using this synergistic effect between two complementary active layers allows for devices with improved contrast between the bleached and colored states while conserving a good overall transparency in the bleached state[3,12]. The addition of the colored states of each layer should yield an esthetically neutral coloration such as dark brown-grey-blue in the case of combined WO_3 and NiO[3].

c) Conventional electrochromic devices

Electrochromic materials can be used within devices to modulate an incident light wave through absorption of the incoming radiation. Such electrochromic devices allow for a large array of usual applications in a number of different fields. Some of these are, for example: electrochromic displays[18], tintable goggles[19], anti-glare rearview mirrors[3], stealth coatings for military use[20] and of course "smart windows"[3].

The typical electrochromic device is composed of five layers arranged in a battery-like configuration (*Figure 6*). An electrolyte is sandwiched between two complementary layers which are in turn sandwiched between two conducting layers[3].

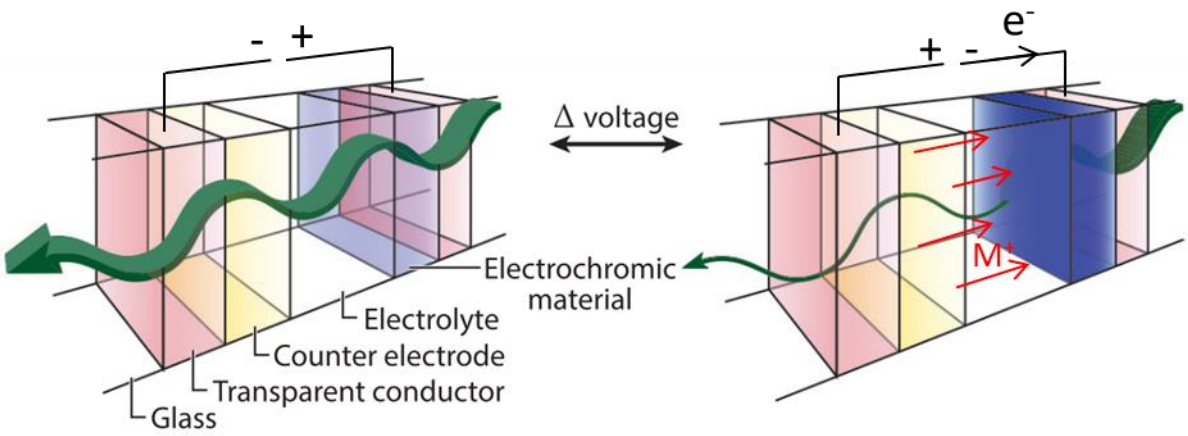

Figure 6: Representation of a multilayered electrochromic device in the bleached (left) and colored (right) state[3].

When a bias is applied, the insertion or extraction of charges into/from the active layers will induce the coloration/bleaching of the device (as previously described in *Section 1.2.b*). The electrolyte acts as an ion conducting media, bringing the ions in contact with one side of the active layer while electrons are brought to the opposite surface of the material through the conductive (sub)layers and the external circuit[3,12].

In order to avoid short circuits the electrolyte should be ionically conducting while electrically insulating at the same time. Also, the electrolyte should be highly transparent in the working wavelength range of the device[12].

The top and bottom conductive layers on both end of the device close the circuit between the electrochromic cell and the potential generator. The two active layers are linked through this external connection, allowing the electrons to travel from one side of the device to the other. In transmittive devices such as “smart windows” both electrodes are required to be highly transparent to allow electromagnetic radiation to be transmitted through the device with minimal loss in light intensity[3].

For such a device to work with optimal efficiency, the active layer and the ion storage layer should be made from complementary cathodically- and anodically-charged materials (cf. *Section 1.2.b*). As the potential is applied, the charges are extracted from the ion storage layer to be inserted in the active layer. The reduction of the cathodic active layer (*Equation 1*) and the oxidation of the anodic ion storage layer (Equation 2) will yield the respective colored states of both layers at the same time. When the opposite potential is applied, the inverted redox reactions will take place, leading to the bleaching of the two complementary active layers[12].

Despite their substantial attractivity, conventional materials exhibit some major drawbacks. First, the coloration/bleaching principle in these materials is based on the reversible insertion and extraction of charges in the host material, as explained in *Section 1.2.a*. However, the deformation accompanying the transfers of alkali ions exposes the crystal lattice to substantial strain, sometimes irreversibly deforming the original material[21, 22]. In addition, the ions inserted into the active layer may be trapped in their insertion sites[23]. These two effects may significantly hinder the quality of the device over time and ultimately shorten its lifespan or “cyclability”. Moreover, the materials used in electrochromic devices do not allow the independent, discrete modulation of visible and IR radiation[3,16], rendering the device sub-optimal from an energy saving standpoint. With the extra ability of independently modulating the different portions of the light spectrum, the savings enabled by a new generation of “smart windows” could be further increased. Indeed, when a warm weather requires a decrease in the amount of heat transmitted into the building (typically in spring and summer) the natural light provided by the sun is blocked as well and artificial lightning is required to overcome this loss of luminosity[3]. Thus, the energy gained from HVAC savings is partially lost due to the energy demand of lighting devices. This lack of selectivity is clearly shown in the colored and bleached spectra of a device made of conventional WO_3 in *Figure 7* below.

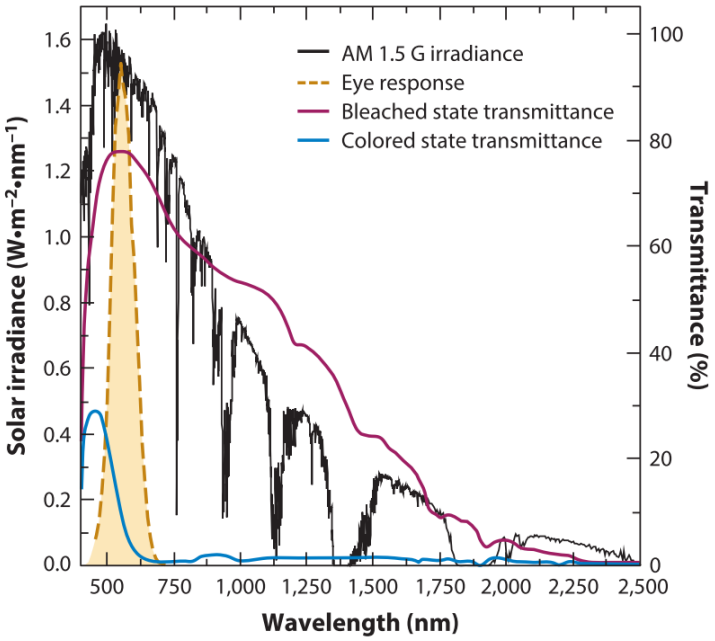

Figure 7: Transmittance spectra of a WO_3-based conventional electrochromic device reported to the solar radiation spectrum at earth surface and the human eye response[3].

1.3. Plasmonic electrochromic materials

Constraints in both durability and specific functionality of conventional electrochromic materials lead to in-depth research in the field and the discovery of a new class of electrochromics designed from plasmonic (nano)materials. Indeed, since more than half of the solar radiation intensity lies in the IR part of the light spectrum[3], highly doped plasmonic semiconductors offer the unique possibility to selectively modulate IR radiation without interfering with the visible light, blocking heat without sacrificing natural lighting during daytime. Simulations have shown that such NIR selective "smart windows" could save up to 167 TWh annually in the United States thanks to major HVAC and lighting savings[3].

a) Principles of LSPR

In conductive materials like metals, holes and electrons behave as a free carrier gas according to the Drude-Lorentz model[24]. In this model, the interactions between electrons are considered to be negligible as well as the interactions between electrons and ions (the latter only being responsible for the charge neutrality of the material). Each electron can thus be considered as an isolated free charge carrier moving in the periodic atomic potential of the crystal lattice as it would do in vacuum[24]. However, for this approximation to be made the mass of the electron must be corrected as an effective mass, calculated from band structures computations and taking the crystal lattice of the material into account (it should be noted that the efficient mass of the free charge carrier could differ greatly from the actual mass of an electron)[24].

In small-size "objects" such as crystalline nanoparticles (NPs), the collective oscillation of free charge carriers can occur following the interaction with an incident light wave (*Figure 8*). If the frequency of the electromagnetic radiation is close to the resonance condition of the material, enhanced light absorption can take place in the nanocrystals (NCs). This oscillation, mainly occurring at the surface of the particles, is known as a surface plasmon resonance (SPR), with the "plasmon" being the quasi-particle resulting from the quantization of plasma oscillations (just as optical oscillations are quantized as photons). In the case of NPs, the resonant wave is confined in the spatially-limited nanostructure and gives rise to a non-propagating standing wave known as a localized surface plasmon resonance (LSPR)[3,16,24,25].

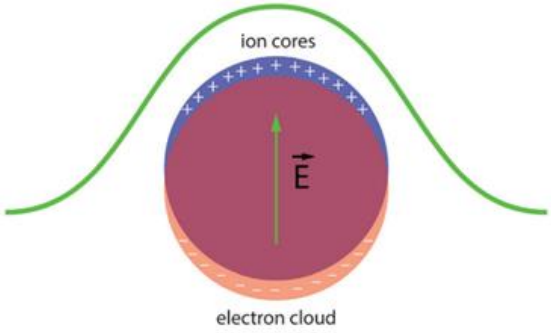

Figure 8: Schematic representation of the interaction between free charge carriers in a plasmonic NC and an incident light wave, giving rise to a localized surface plasmon[16].

The ability of metal NCs to support LSPR, arising from their high free charge carrier concentration ($\simeq 10^{22}$ cm^{-3}), is well known[24]. The Drude-Lorentz model of the dielectric permittivity in materials containing free carriers can be described by the following formula (*Equation 3*):

$$\varepsilon = \frac{\varepsilon_\infty - \omega_p^2}{\omega^2 + i\gamma\omega} \qquad (3)$$

With ω the frequency of the incident radiation, ω_p the plasma frequency, ε_∞ the background dielectric constant and γ the damping parameter, describing the frequency of occurrence of scattering phenomena[24].

The plasma frequency is defined as *Equation 4*:

$$\omega_p = \sqrt{\frac{ne^2}{\varepsilon_0 m_e^*}} \qquad (4)$$

With n the concentration in free charge carriers, e the charge of the electron, ε_0 the vacuum permittivity and m_e^* the efficient mass of the charge carrier[16,24].

However, several conditions must be met for the observation of a LSPR signal using this model. First, the concentration in free charge carriers should be sufficient for the material to display a metallic behavior[24,26]. Then, the size of the particle should lie in a range in which the electronic structure of the particle is similar to that of the bulk and the dielectric polarization is uniform in each particle. Generally, this range includes particles just larger than a few nanometers and smaller than one fifth of the LSPR wavelength[26].

Since the resonance frequency of the plasmon depends on the free carrier concentration (cf. Equation 3), the plasmonic response of metals lie in the visible part of the light spectrum[24]. However, for them to be relevant as IR selective materials for a new generation of "smart windows", larger metallic particles (> 200 nm) and/or complex morphologies would be required to shift the resonance in the infrared (IR) range[27-30]. This enlargement of the particles could make them impracticable if their size does not meet the size requirements of the Drude-Lorentz model for the particle to support LSPR anymore.

One the other hand, highly doped nanocrystalline semiconductors are another class of materials that can support LSPRs. Due to the fact that their concentration of free charge carriers is lower than that of metals ($10^{19\text{-}21}$ cm^{-3}), most of these materials exhibit plasmon resonances in the mid to near-IR region[24]. In addition, the spectral position of the plasmonic absorption in highly doped semiconductors can be finely tuned depending on the amount and distribution of doping of the material. This modification of the doping level in the compound can be achieved in-situ, during the synthesis by chemical doping, but also post-synthesis from photochemical and/or electrochemical bias of the material[24].

b) LSPR and plasmonic electrochromism in transparent conducting oxides

In the metal oxides class, several highly-doped metal oxides known as "transparent conductive oxides" (TCOs) have been shown to support plasmonic resonance. The corresponding electrochromic properties of this class of materials have been observed for the first time in 1999 when Boschloo and Fitzmaurice pointed out the electrochromic charging of antimony-doped tin oxide (ATO)[26]. Since then, many advances have been made in this research field, one of them being the development of an electrochromically-efficient form of nanocrystalline tin-doped indium oxide (ITO) by Milliron *et al.* in 2011[31], leading to the design of NIR-selective thin films and devices.

In their work, they specifically highlighted the pseudocapacitive nature of the electrochromic charging behavior. Pseudocapacitve materials exhibit the same electrochemical signature as capacitive materials, such as activated carbons (i.e. linear dependence between the charge stored and the applied potential within a given range of work potential). The difference between these materials lies in their charging mechanisms, with pseudocapacitive compounds relying on electron-transfer mechanisms rather than on the insertion of ions into the lattice of the material[32]. This charging behavior in plasmonic compounds was

anticipated from similar observations previously noticed in other plasmonic materials such as Ag aggregates[33] and colloids[34], ATO nanocrystals[35], CdSe quantum dots[36]and Au nanorods[37] (and has also been shown in new materials such as $Cu_{2-x}Se$ in recent years)[38].

Since the resonance frequency of the LSPR depends on the level of doping of the material, the spectral position of the LSPR absorption can be either red-shifted or blue-shifted throughout a given spectral range by decreasing or increasing the amount of doping, respectively. This can be done by the application of an appropriate electrical bias, leading to injection/removal of charge carriers into/from the particles and thus modifying the concentration of free charge carriers in the material. This effect can be deduced from Equation 3, in which the interdependence between the plasmon frequency and the square root of the concentration in free charge carriers is explicit. Also, the optical blue/red-shift depending on the concentration in free charge carriers is shown in *Figure 9* below.

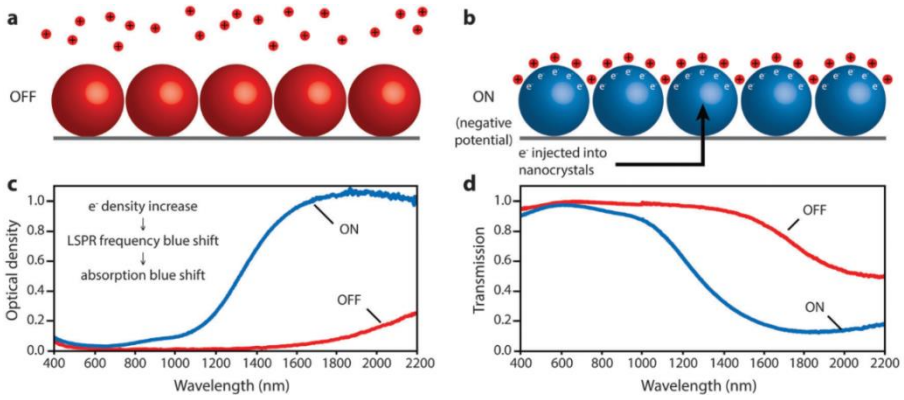

Figure 9: Representation of the pseudocapacitive charging mechanism of plasmonic materials in a) the bleached state and b) the colored state and the corresponding evolution of optical density (c) and transmission (d) curves[16].

In addition to the original description of the NIR electrochromic behavior of ITO NCs, Milliron and her co-workers could highlight their superior optical and electrochemical properties such as a deep and tunable modulation in a relevant spectral range for “smart windows” applications, high coloration efficiency and exceptional life expectancy (> 20k charge/discharge cycles)[31]. Their work was a crucial milestone in addressing successfully both the durability and functionality limitations of conventional active materials, allowing for the development of a new generation of electrochromic materials and devices.

In a second time, efforts have been put in order to optimize the spectral limitations of such TCOs. Indeed, due to the fact that most of the infrared light emitted from the sun lies in a spectral region comprised between 750 and 1250 nm, the plasmonic response of highly doped TCOs does not provide enough spectral efficiency, as optical modulation is provided in a large interval of wavelength starting from ITO at around 1600 nm up to AZO at 4000 nm and ATO going as high as 5000 nm[26,39]. In this region, the intensity of infrared solar light is

definitively lower and almost becomes negligible as one follows the wavelength axis up to ATO and materials alike (as it can be observed in the far right section of *Figure 10*, the solar spectrum appears to be extinct at such high wavelengths).

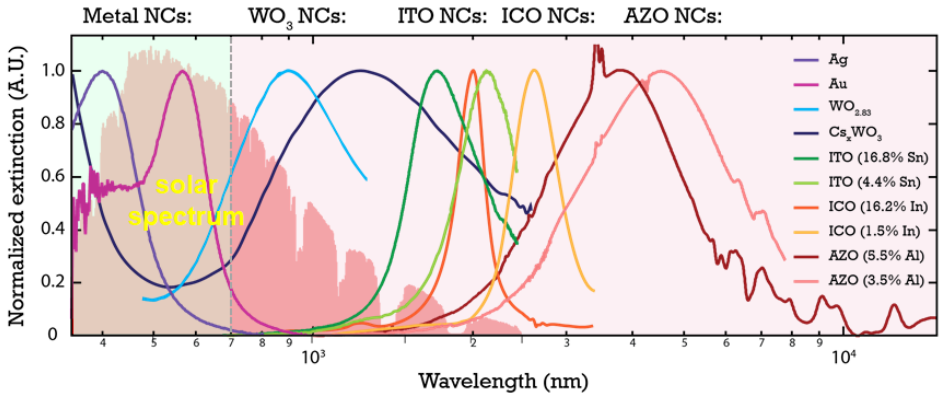

Figure 10: LSPR signals of several metal and semiconduting plasmonic materials, reported to the solar spectrum in the background of the figure[39].

To sum up, electrochromic devices based on conventional materials are limited to only two modes: the clear and dark modes (cf. *Section 1.2.a*). In the former, both visible and IR light are transmitted through the material, while in the latter the polaronic absorption of the active layer impacts visible and IR radiation at the same time, switching the material into its low transmission state. However, the recent development of plasmonic materials brought along a new type of functionality in the field of electrochromics: dual-band, 3-modes "smart windows".

c) *Towards dual-band electrochromism: independent modulation of VIS and NIR ranges*

Indeed, by associating a conventional material to a plasmonic one, it is possible to produce a device able to specifically modulate visible and infrared light independently. Such a device was also developed by Milliron *et al.*, combining ITO plasmonic nanoparticles dispersed in a matrix of electrochromically active NbO.

At a given potential, none of the materials are activated and the device is fully transparent, allowing both visible and NIR light to be transmitted. As the potential decreases, the material will be gradually charged in a capacitive manner, thus activating the plasmonic response of ITO. In this new configuration, visible light is still allowed to be transmitted through while heat (NIR radiation) is retained by the plasmonic material (cool mode). Finally, if the applied bias is further decreased, it will become low enough to actually reduce the conventional NbO matrix through the faradic insertion of charges into the host lattice (and consecutive reduction reaction). In this case, the device acts the same way conventional electrochromic devices do, blocking both visible and infrared light in the colored mode (dark mode)[40] (*Figure 11*).

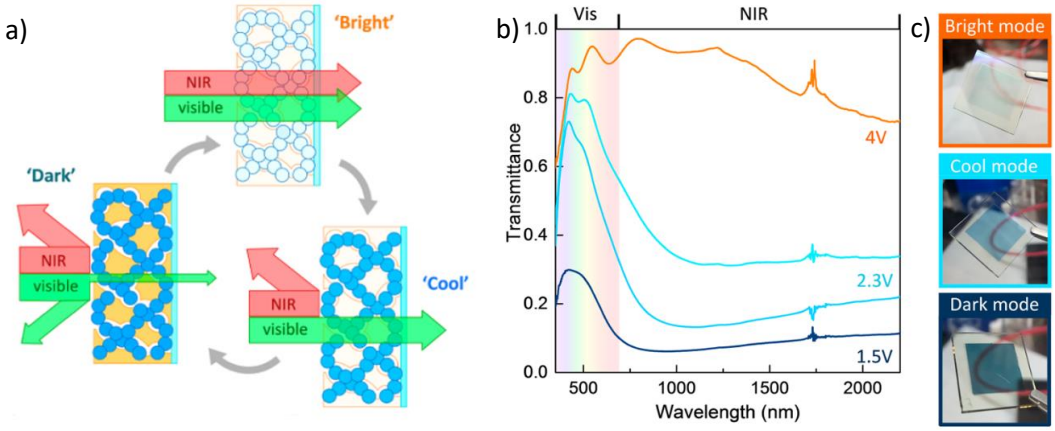

Figure 11: a) schematic representation of the principle of a dual-band electrochromic "smart window", b) the corresponding transmittance curves and c) actual pictures of the film in each state[40].

However, for economic reasons and manufacturing simplicity, the quest for new and more efficient plasmonic materials is still of great interest. Founding a three-way single material with properties comparable to those of the combined ITO-in-NbO_x devices would allow for a simpler and more cost-efficient new generation of plasmonic smart windows.

Since the plasmonic properties of such a material should be able to overlap the visible and IR region of the spectrum, first generation TCOs like ITO are not able to modulate light in this 3-way fashion on their own. In order to obtain NIR-selective compounds of higher efficiency presenting a LSPR wavelength range approaching the 750-1250 nm region of interest, new materials have been proposed and studied. Among this new generation of plasmonic materials, oxygen vacancy-doped tungsten oxide WO_{3-x}, whose LSPR signals stand around 900 nm[3, 26,39,41].

In oxygen-vacancy doping, the electrons that would normally be implied in a metal-oxygen bond are now free charge carriers allowing the material to support LSPR. However, there is a threshold to the amount of oxygen vacancies (the "x" value in WO_{3-x}) under which the material will not exhibit any plasmonic properties. For example in WO_{3-x}, the minimal value of x is 0.1. When the material is doped over this limit it will go through a semiconductor-metal transition in which the amount of free charge carriers is large enough to degenerate the electronic structure from a semiconductor configuration to a metal one. For any values of x lower than the 0.1 threshold, the absorption mechanism of the material will be dominated by conventional polaronic absorption[41].

The other proposed material is alkali-doped WO_3 (e.g. Cs_xWO_3[16]) with a plasmonic frequency of 1000-1100 nm[39]. In this case the material is obtained from the aliovalent interstitial doping of WO_3 by alkali ions, yielding the corresponding tungsten bronze. As alkali Cs ions are inserted into the crystal lattice of the oxide, some of the W metallic centers are reduced from W^{6+} to W^{5+}, eventually increasing the concentration of free charge carriers in the compound.

Given the position of these LSPR peaks, almost overlapping the visible and infrared regions, and the possibility to either blue-shift or red-shift the signal by increasing/decreasing the concentration in free charge carriers, respectively, these new generation materials are able to independently modulate both visible and NIR light. Similarly to the dual band ITO-in-NbO_x devices, the optical properties of WO_{3-x} can be tuned to cover a given range of wavelength across the light spectrum (*Figure 12*). In the bright mode, the LSPR signal of the oxide is red-shifted deep into the infrared region, too far to efficiently modulate any incident radiation. As the potential decreases, more electrons are injected in the active layer, thus blue-shifting the LSPR in a region where the NIR intensity in the solar spectrum is intense enough to efficiently modulate the amount of heat transmitted through the device (cool mode). Further decrease in the applied bias will actually reduce the material through the faradic insertion of charges into the host lattice (and consecutive reduction reaction). In this case, the material acts the same way conventional electrochromics do, blocking both visible and infrared light in the colored mode (dark mode).

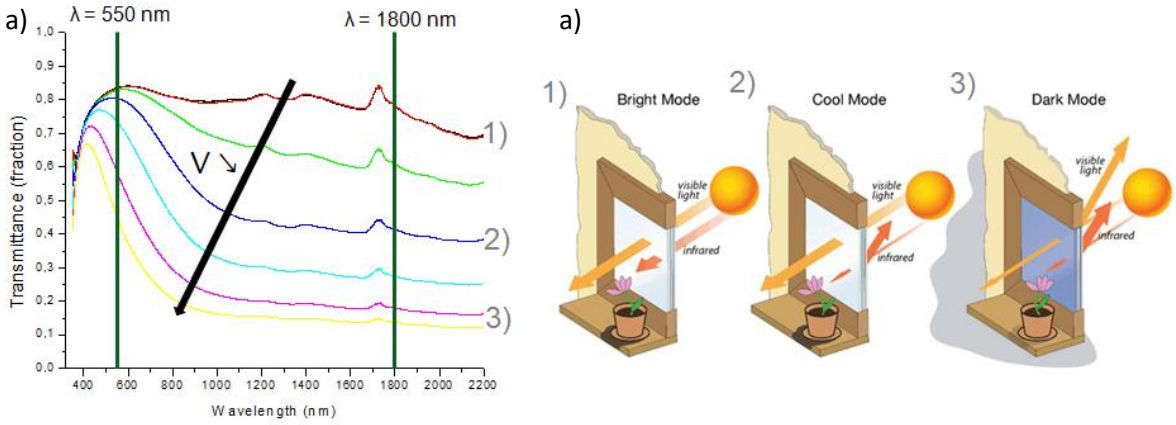

Figure 12: Transmittance spectra at varying potentials[42] (a) and representation of the device[43] (b) of a single material dual-band electrochromic based on sprayed plasmonic tungsten oxide in the bright (1), cool (2) and dark modes (3).

d) *Molybdenum-tungsten hybrid oxide: the new generation of plasmonic electrochromic materials?*

Considering novel and optimized forms of WO_{3-x}-based nanomaterials, molybdenum tungsten hybrid oxide appears to be one of them. In a recent publication from Yamashita et al.[25], it was shown that a vacancy-doped molybdenum tungsten hybrid oxide ($Mo_yW_{1-y}O_x$, further labeled "$MoWO_x$" in this work) could also exhibit LSPR in the red-end of the visible range (600-700 nm) but crucially several times more intense than that of the "pure" oxides MoO_{3-x} and WO_{3-x} (*Figure 13*), respectively displaying a 20 and 16 fold increase in absorbance[25].

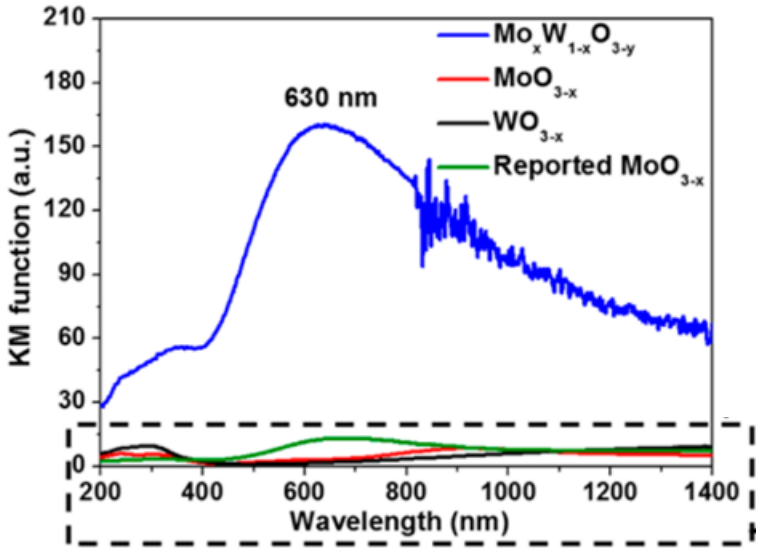

Figure 13: Diffuse reflectance spectra of $MoWO_x$ hybrid compared to pure Mo and W oxides (framed by the dotted line), transformed into absorbance curves using the Kubelka-Munk function[25].

Such materials have been studied in the context of heterogenous catalysis, in comparison with other bimetallic hybrid materials such as Co-Mo-N, Fe-Ni-P and Ni-Mo-S have recently brought a lot of attention because of their exceptional properties for reactions[25] like oxidation, hydrogenation and hydrogen evolution, but also as light harvesting materials[25, 44-47]. The growing interest in the coupling of different components arises from its possibility to lead to superior performances due to a synergistic effect between the materials. On one hand, the modification of the surface properties and morphology can lead to the exposure of a larger number of active sites. Meanwhile, the intrinsic electronic structure of the hybrid can be tuned by the hybridation process to lead to a more efficient material[25].

According to Yamashita and his co-workers, in the case of $MoWO_x$ the sudden improvement in the spectral response of the material is due to two main effects, both leading to the formation of crystal defects ultimately leading to a greater LSPR intensity. The first one is the mutual doping of the Mo and W ions, forming a solid solution of both oxides. The $MoWO_x$ crystallites are organized into layered edge-sharing and corner-sharing octahedrons of MoO_3 and WO_3. During the reaction, as W ions are inserted in the MoO_3 crystals and vice-versa, the inherent deformation of the lattice obviously leads to huge symmetry disturbances and modifications of the electronic structure of the material. On the other hand, the intercalation of hydrogen atoms from the H_2O_2 and isopropanol used as reactant / solvent in the synthetic process (see Chapter 2 below) could disturb the charge neutrality of the crystal, resulting in the reduction of neighboring metallic centers into W^{5+} and Mo^{5+}. In addition, the reductive properties of H_2O_2 and isopropanol could also lead to the formation of oxygen vacancies during the synthesis of the material[25].

Therefore, the combination of the mutual ionic substitution to form a solid solution and the formation mechanism of oxygen vacancies is expected to lead to a massive increase in the concentration of available free charge carriers in the material, eventually leading to the greatly enhanced LSPR observed in the hybrid oxide (*Figure 14*).

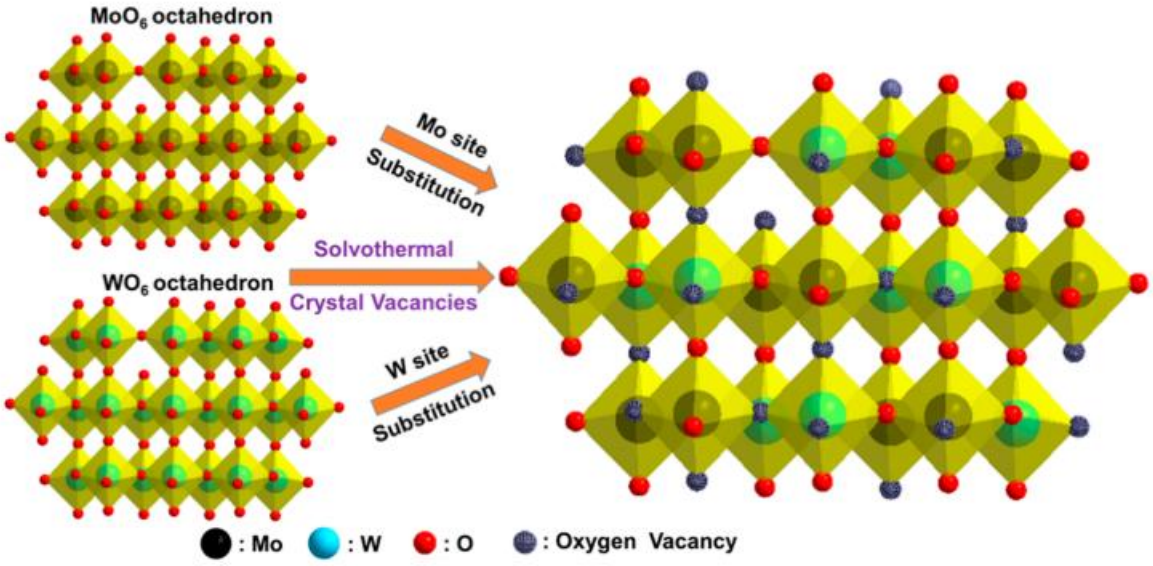

Figure 14: Proposed formation mechanism and crystalline structure of the molybdenum tungsten hybrid material[25].

While plasmonic $MoWO_x$ nanoparticles has already been reported in the literature as a water splitting catalysis agent[44], light harvester[47] and shows promising properties for application as a battery material[48], it has never been used as a plasmonic electrochromic material to the best of our knowledge – even if stoichiometric molybdenum tungsten hybrid oxide $Mo_yW_{1-y}O_3$ has been reported as such recently. Several previous publications by Li *et al*.[49,50] and Gesheva *et al*.[51] have highlighted a stronger electrochromic effect and higher coloration efficiency displayed by the hybrid $MoWO_3$ in comparison to the pure oxides as a result of the hybridation of the material. Therefore, it is expected that the oxygen deficient form of material similarly displays superior properties to that of sub-stoichiometric pure oxides.

The great absorption signal displayed by this material and the position of the LSPR it supports (overlapping both the visible and near infrared regions of the spectrum) make of "$MoWO_x$" coumpounds materials of choice for the development of a highly efficient new generation 3-way electrochromic device able to discretely modulate visible and infrared radiations.

1.4. Objectives of the present work

In this work, various experimental approaches of chemical synthesis, structural and optical characterization are used to establish and discuss the occurrence of a plasmonic electrochromic behavior in thin films of molybdenum tungsten oxide $Mo_xW_{1-x}O_{3-y}$ "$MoWO_x$" nanocrystals.

Specifically, $MoWO_x$ nanocrystals are generated from a solvothermal synthesis process, exploiting the experimental protocol previously reported by Yamashita et al. First, the influence of the synthesis conditions, namely the ratio of W and Mo precursors, on nanocrystals size, shape, crystallinity and composition is systematically investigated and discussed from microscopic analyses (scanning electron microscopy SEM, transmission electron microscopy TEM), X-ray diffraction (XRD) and inductively coupled plasma – optical emission spectrometry (ICP-OES) measurements. The optical properties of the synthesized materials, especially their plasmonic behavior, are also analyzed using UV-VIS-NIR spectrophotometry in reflectance mode.

In a further step, attempts to find the best conditions for the colloidal dispersion of the differents $MoWO_x$ NCs are conducted. Various conditions of dispersions (solvent, concentration, incorporation of additives …) are tested and progressively refined in order to deliver the most appropriate inks to be further deposited as thin films onto transparent conductive glass substrates. Two sorts of wet deposition methodologies are used at this purpose: spin coating and bar coating. Ultimately, the films functionality in terms of electrochromic behavior is qualitatively investigated using electrochemical methods.

Chapter 2 – Synthesis and characterization of MoWOx nanocrystals obtained from solvothermal protocols

2.1. Solvothermal synthesis of $MoWO_x$ NCs

a) General principles

In order to synthesize this unique hybrid nanostructured material, we consider a protocol previously reported by Yamashita and co-workers, using a non-aqueous solvothermal route in absence of surfactants.

Hydro- and solvothermal syntheses are very similar, the only difference between them lies in the choice of the reaction medium, respectively being either water or organic solvent. In both cases, the starting materials are placed in a polytetrafluoroethylene vessel (PTFE or Teflon®). This container is sealed in a stainless steel autoclave which is then exposed to thermal treatment at a given temperature for a certain duration. Exploiting the auto-generated pressure in the autoclave, highly-crystalline nanoparticles can be produced with a high degree of control on size, shape and composition as well as excellent dispersity and stability features[52]. Finding the right synthetic parameters is essential for the outcome of the experiment to meet the expected physicochemical properties of the product.

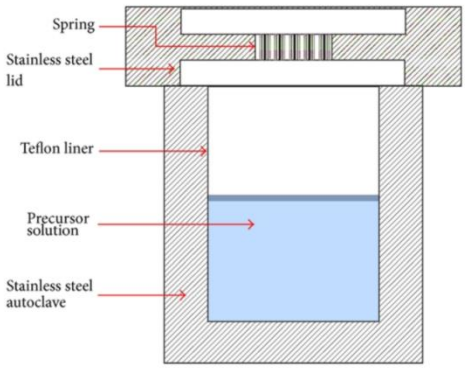

Figure 15: Schematic representation of a hydrothermal/solvothermal stainless steel autoclave containing the PTFE vessel[53].

The main benefits of this method, compared to the usual surfactant-assisted colloidal synthesis route under inert conditions (Schlenk line), are the simplicity of the equipment and its ease of use even for non-experienced operators, in addition to the possibility to synthesize nanostructured particles in a “surfactant-free” fashion as well as the up-scaling potential of the method. However, this technique acts as a “black box”, the reactants being placed and sealed in the autoclave and the products recovered at the end of the process without knowing the exact reactions taking place inside the vessel.

b) Materials and methods

Molybdenum powder (Merck KGaA, 99+ %), tungsten powder (Merck KGaA, fine powder 99+ %), isopropanol (Acros, 99.5+ %, extra pure), ethanol (VWR, technical), poly(ethylene glycol) (Sigma Aldrich, M = 140000) and poly(ethyleneimine) (Sigma Aldrich, M = 750000, 50 %wt. in H_2O) were all used as purchased without further purification. The substrates were made on fluorine doped tin oxide (FTO) coated glass (PG Fast 15 Ohms/square, 4 mm thick).

For the synthesis of the active materials, we adapted the method used by Yamashita et al.[25] Briefly, a constant total of 1.5 mmol of starting reactant (Mo and W powders) was kept throughout the different synthesis. These 1.5 mmol of metallic powder are dissolved in 1.88 mL of H_2O_2 and the solution is stirred for 1 h to allow the completion of the dissolution reaction. Then, 11.25 mL of isopropanol is added to the mixture and stirred again for only a few seconds for homogenization. For the following step, the solution is placed in a 17 mL PTFE vessel which is then sealed in a stainless steel autoclave. The container is kept in oven at 160°C for 12 h then cooled down to RT. At the end of the thermal treatment, the obtained dispersion is centrifugated at 10000 RPM to collect the solid particles and rinsed with ethanol three consecutive times. Finally, the powder is dried overnight in a vacuum furnace at 50°C.

Using this method we synthesized a molybdenum/tungsten hybrid oxide in three different Mo/W ratios (Mo/W = 2/1, 1/1, ½) as well as the "pure" substoichiometric oxides of both Mo and W. In this work, these materials will be referred to as "$MoWO_x$ 2:1", "$MoWO_x$ 1:1" and "$MoWO_x$ 1:2", directly depending on the molar ratio of Mo and W starting materials used for the synthesis. One the other hand, MoO_{3-x} and WO_{3-x} simply correspond to the chemical formulas of the oxygen vacancy doped oxides.

c) Solvothermal synthesis of $MoWO_x$ NCs

The solvothermal process used in this work allowed us to recreate the material synthesized in the reference publication exhibiting similar properties.

First, the reaction between the metallic powders and H_2O_2 yields a bright yellow solution in an exothermic reaction accompanied by the production of gas. The oxidation kinetics of the powders differs greatly, with Mo leading to a more aggressive instantaneous reaction, producing more heat and gas in the first few seconds than the slowly reacting tungsten powder.

The oxidation of the precursor into the hydrated peroxide complexes MoO_2 (OH)(OOH) and WO_2 (OH)(OOH) results in a stable solution[25]. Next, the dehydration of these species during the solvothermal treatment leads to the formation of Mo-W hybrid nuclei. These nuclei are the starting point for the intrinsic growth into nanorods. In addition to the reductive nature

of isopropanol, the anisotropy of the growth presumably owes to the layered crystal structure of the oxides, leading to the formation of $MoWO_x$ nanorods[25].

At the end of the solvothermal process, we recover a dark blue dispersion in the case of the hybrids while the pure oxides lead to lighter, gray blue suspensions. This characteristic coloration has been shown in many deficient transition metal oxides (such as TiO_{2-x} and WO_{3-x}) as this property arises from their typical outer d-shell electrons[25].

The different steps of the synthetic process are presented in the following *Figure 16*, with pictures showing the appearance of the reactive media for each corresponding steps.

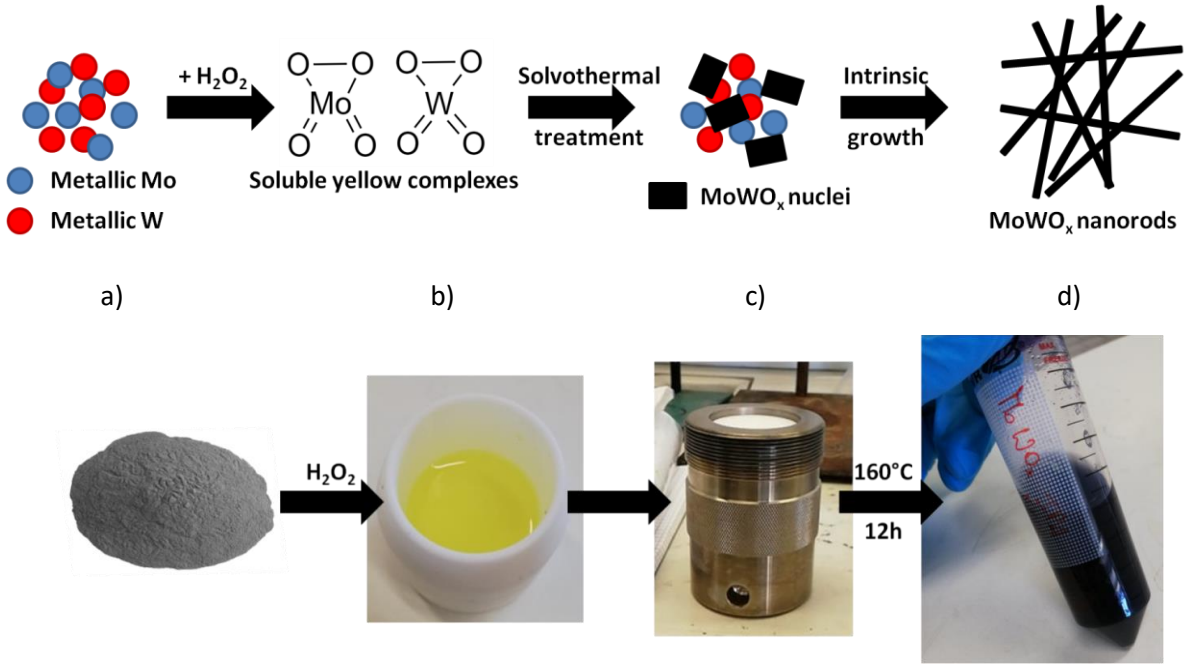

Figure 16: Schematic representation (top) and pictures (bottom) of the different steps of the solvothermal synthetic process: a) metallic powders, b) dissolution into yellow soluble complexes, c) formation of $MoWO_x$ nuclei and d) preferential growth into nanorods.

d) MoWOx NCs : morphology and crystallinity

The powders recovered after drying of the solvent were characterized using several techniques. Morphological properties (size, shape, structures) were observed using transmission electronic microscopy (TEM) and scanning electron microscopy (SEM). Micrographs at different magnifications were obtained on a JEOL JEM1400 (TEM) and a Philips XL30 ESEM FEG (SEM).

The morphologies of each material are represented in *Figure 17* (TEM) and *18* (SEM). The different Mo/W ratios all appear to yield similar looking particles, as nanowires or nanorods, aggregated in larger micronic particles for the majority. These nanoparticles can also be found in needle-like formations consisting in a few particles aggregated and often displaying a preferential orientation, with the biggest nanorods all oriented in a similar fashion (inset in

Figure 17.c). However, in $MoWO_x$ 12, and especially in the SEM imagery, we notice the presence of micron-sized hexagonal clusters being much bigger than the hybrid $MoWO_x$ material and only found in the Mo/W : 1/2 powder. These particles are further investigated to better understand their nature and the reasons behind their specific occurrence for only one of the ratios and the synthetic processes involved in their formation.

While the 3 different $MoWO_x$ exhibit comparable size and shape, it is far from being the case with the pure oxides. Both MoO_{3-x} and WO_{3-x} particles are µm-size and present a well-defined, uniform shape and size distribution. The MoO_{3-x} particles look like flat, elongated and narrow pellets, almost "feathery" looking while WO_{3-x} adopts a hexagonal configuration similar to what is observed in the Mo/W : 1/2 hybrid. Therefore, we presume that these particles are in fact additional WO_{3-x}, formed during the synthesis from the excess of metallic tungsten in the initial reactant mixture.

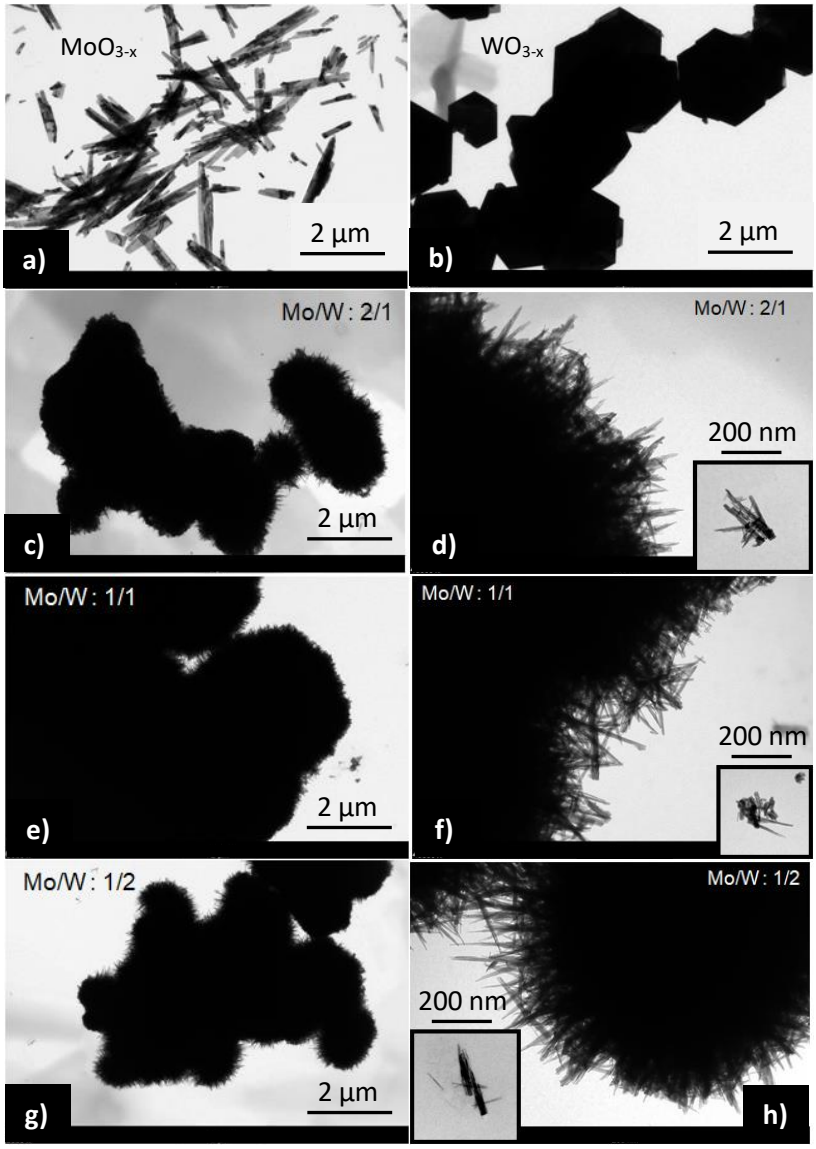

Figure 17: TEM micrographs of: a) MoO_{3-x} particles, b) WO_{3-x} particles, c) $MoWO_x$ 2:1 aggregates and the same image at a greater magnification (d) with a needle-like formation in inset, e) $MoWO_x$ 1:1 and f) the corresponding magnification, g) $MoWO_x$ 1:2 and its magnified image (h).

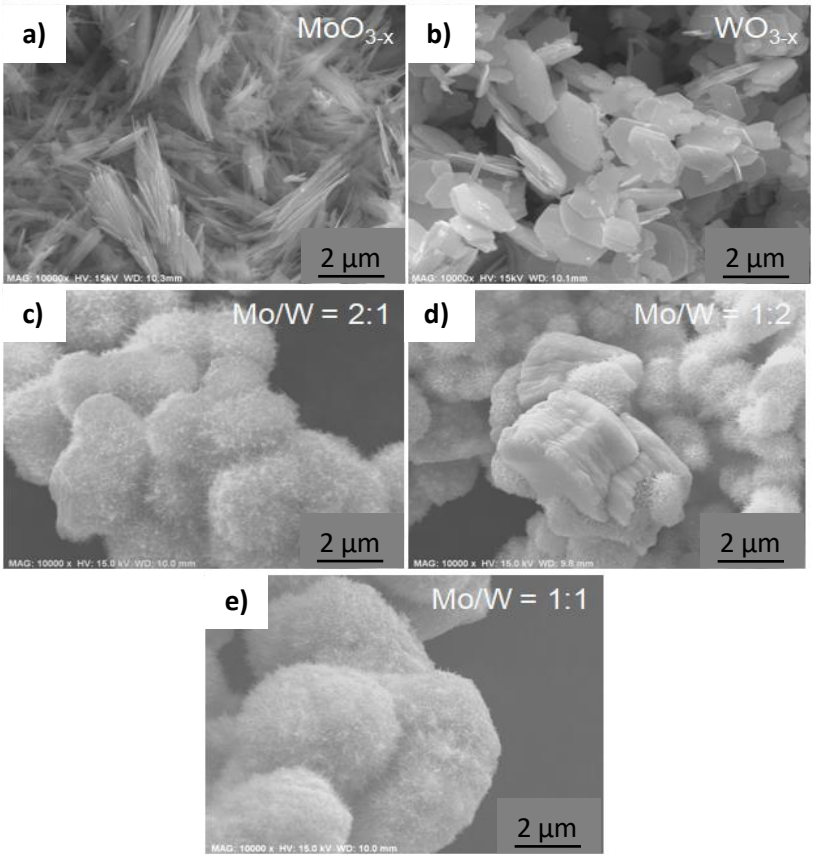

Figure 18: SEM micrographs of the synthesized powders: a) MoO_{3-x}, b) WO_{3-x}, c) $MoWO_x$ 2:1, d) $MoWO_x$ 1:2 and e) $MoWO_x$ 1:1.

The mean lengths of the particles are determined by statistical measurement over a population of n = 50 on the basis of the TEM micrographs, a rough estimation of their width is indicated for information. The results are summarized in *Table 1*. The standard deviations were computed for each compound and used for the determination of the corresponding confidence interval. Since the sample size were rather limited (n = 50), we used Student's t-distribution[54], estimating the 95 % confidence intervals using Equation 5:

$$\bar{X} \pm t_{n-1} \qquad (5)$$

With $\bar{X}$ being the mean value, n the number of elements in the population, S the standard deviation and t_{n-1} a statistical parameter depending on the degrees of freedom (n-1) and the required precision over the measurement (confidence is set to 95 % in the present case).

While the pure oxides are clearly larger than the hybrids, the values show no significant size variations between the different ratios, indicating the independence between these two parameters.

	Mean size (nm)	Standard deviation	95 % confidence interval	Estimated width (nm)
MoO_{3-x}	1384	544	± 155	100
$MoWO_x$ 21	90	42	± 12	20
$MoWO_x$ 11	92	52	± 15	20
$MoWO_x$ 12	83	37	± 11	20
WO_{3-x}	1863	475	± 135	1800

Table 1: Statistical measurement of the particle size of MoO_{3-x}, WO_{3-x}, $MoWO_x$ 2:1, $MoWO_x$ 1:2 and $MoWO_x$ 1:1

e) Crystallinity

The crystallinity of the material is studied using X-ray diffraction on a Brucker D8 X-ray diffractometer. The diffractograms are measured between 2θ values of 5° and 90° with a 0.02° step width and a 0.2 s step time for a total of 15 minutes of measurement.

The pure oxides (*Figure 19*) display results in good adequacy with the theoretical diffraction patterns of the materials. The crystalline structure of our WO_{3-x} corresponds to hexagonal WO_3, which is in accordance with the shape observe in the micrographs of the powder. MoO_{3-x} on the other hand, seems to correspond to a mixture of monoclinic and ortorhombic phases.

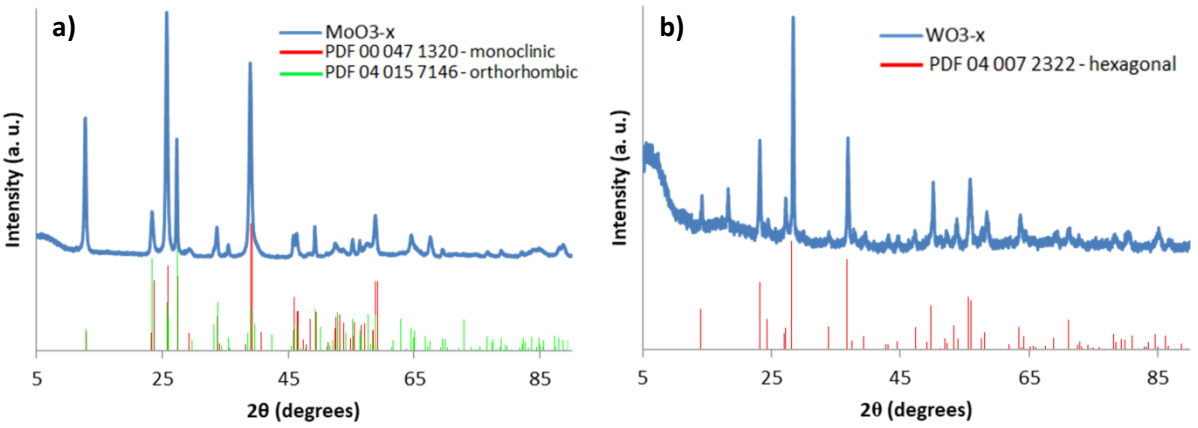

Figure 19: Diffractograms of the pure oxides: a) MoO_{3-x} and the corresponding monoclinic and orthorhombic reference XRD patterns, b) WO_{3-x} and hexagonal PDF reference pattern.

In the case of the hybrids (*Figure 20*), we obtain results very similar to what was published in the reference publication by Yamishita et al. The diffractograms of the three hybrids display 2 main peaks located at 2θ = 23° and 47°. Although peaks corresponding to residual metallic powder were observed in the reference work, this is not the case for our powders. Therefore, we might have achieved a higher conversion yield.

The two peaks observed in hybrids at 23° and 47° can also be found in the diffracting pattern of WO_{3-x}, indicating that the structure of the hybrid is mainly based on that of the tungsten oxide. However, those two peaks are the only one expressed in the $MoWO_x$ powders. This could be the result of the preferential growth along the (002) plane of hexagonal WO_3 (2θ = 23°)[25], resulting in the formation of nanorods. However, in the special case of $MoWO_x$ 12, the whole WO_{3-x} diffraction pattern can be observed on top of the typical shape displayed by the hybrids. This indicates the presence of an excess in tungsten oxide in the powder, in accordance with the observations made in the previous micrographs (cf. *Figure 18.d* in *Section 2.1.d*). Noteworthy, such behavior was not observed by Yamishita et al. in their reference study, instead, the excessive tungsten remained as metallic powder instead of forming oxides.

From these observations, it appears that a maximal amount of W can be inserted into the hybrid structure before saturation. Once the concentration in tungsten surpasses this limit, the remaining tungsten reacts to form pure WO_{3-x} oxide. This effect is not observed in the case of Mo within the working ratios used in this work. This observation could be the results of many factors. First, the kinetics of each powder varies greatly, as explained in the case of their oxidation. Then, the formation mechanism of the crystal has a key role in the formation of the excess tungsten oxide. Since the structure of the hybrid is closer to WO_{3-x} than it is from MoO_{3-x}, it could be assumed that the ionic substitution preferentially occurs for the insertion of Mo in a WO_{3-x} lattice base. In that case, an excessive amount of WO_{3-x} would be formed while the available quantities of Mo are not sufficient to substitute the additional tungsten oxide, leading to the formation of a “heterogeneous” hybrid oxide.

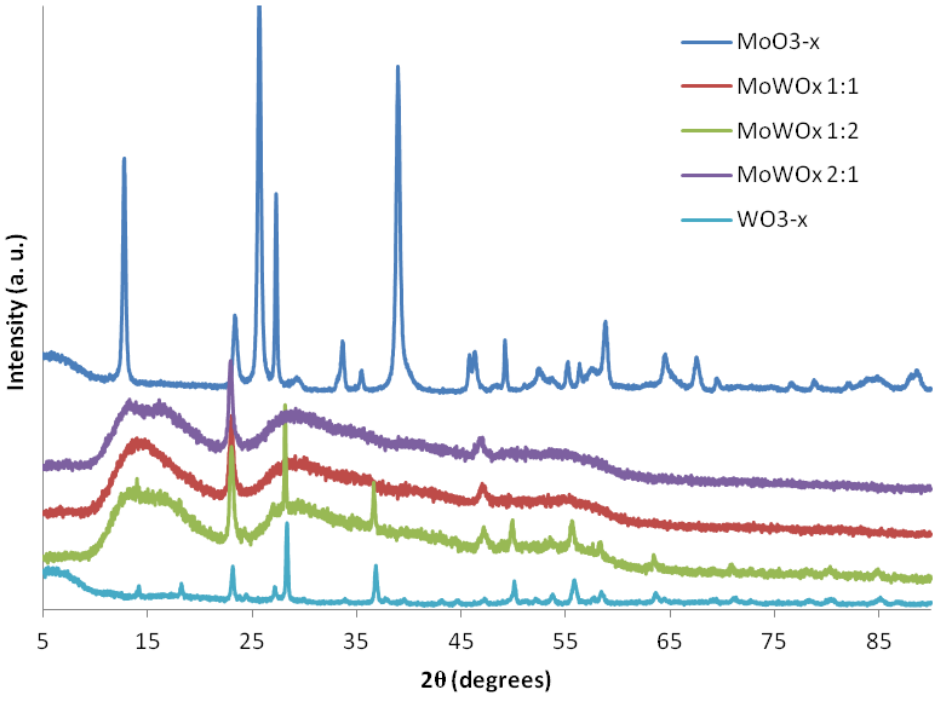

Figure 20: Comparison of the diffractograms of all 5 powders.

f) Composition

The Mo/W molar ratios of the three hybrids were determined using ICP-OES. The results can be found in *Table 2*. Here, we can see that the initial ratios in precursor material are well conserved after the synthesis of the product with similar results using both techniques.

Initial Mo/W ratio	Mo (mol/mL)	W (mol/mL)	Final Mo/W
2/1 = 2.00	0.16	0.08	1.92
1/1 = 1.00	0.11	0.11	1.03
1/2 = 0.50	0.09	0.14	0.64

Table 2: ICP-OES measurements of the molar ratios in the hybrids. The initial ratio is calculated from the precursor ratio used for the synthesis, the final ratio is calculated from the ratio of the concentrations determined by ICP-OES measurements.

These ratios were also determined using EDX measurements (cf. *Annexes I.b*). However, as EDX is a semi-quantitative technique while ICP-OES is quantitative, the results recovered from the latter tend to be closer to reality. In addition, the main Mo ray overlaps a secondary W ray in EDX, which may bias the exact value of the measurement if not correctly fitted. One can observe the difference between the results obtained by both methods increases as the concentration in W increases. For these reasons, the ICP-OES values are considered as more precise. Nevertheless, EDX can be used to have a vague idea of the final ratio in the powders if it differs enough and as a less time-consuming method (no preparation of standard solutions required, no calibration of the pipette). However, if precision is required and time is not a limitation, we would advise to use ICP-OES if possible given the advantages brought with this technique.

g) Optical properties : reflectance measurements

Reflectance measurements on the powders showed results in accordance with their expected behavior. Reflectance measurements of the powders were realized on a Shimadzu UV-3600 Plus using an integrating sphere. $BaSO_4$ was used as the reference material for the measurement of the baseline. A small amount of powder (either the $BaSO_4$ reference or one of the synthesized oxides) was placed in a sample holder and analyzed. The recovered reflectance data were converted into absorbance measurements using the Kubelka-Munk function, used as a mathematical tool used to correct the intensity of the different peaks in a reflectance spectrum to yield what could be considered an absorbance signal[25,55].

As presented in the reference work by Yin et al., the reflectance displayed by our hybrids was greater than that of the pure oxides by more than an order of magnitude. The

absorbance spectra of the five synthesized products, obtained by transformation of the reflectance spectra using the Kubelka –Munk fuction, can be found below in *Figure 21*.

The pure oxides display weak asymmetric LSPR signals centered around 700 nm while the oxides are characterized by a large peak located at 600 nm, showing the expected blue shift arising from the hybridation process (cf. *Section 1.3.d*).

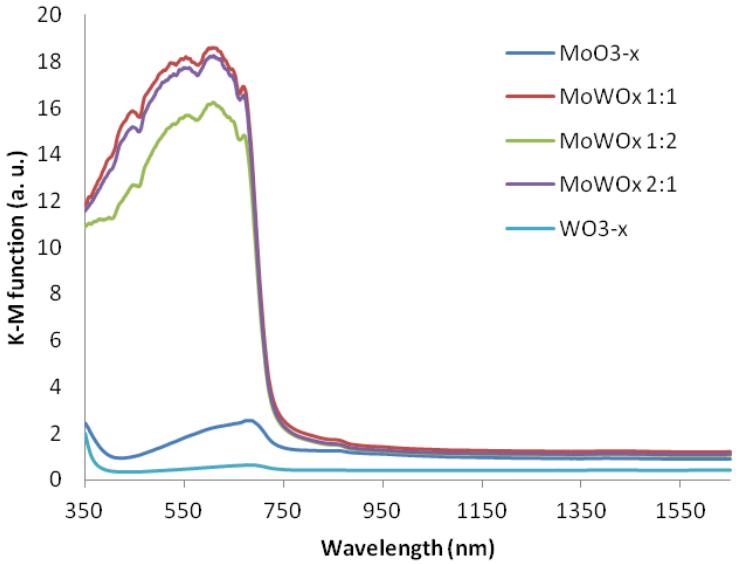

Figure 21: Absorbance spectra of the five powders, obtained from the transformation of diffuse reflectance measurements using the Kubelka-Munk function.

Even though the overall expected tendencies in the optical behavior of the powders are observed, the spectra are oddly shaped. Indeed, all the measurements exhibit a sudden drop in intensity around 700-800 nm. Since this loss in signal is observed throughout all the solid samples independently of their nature, we figured the issue probably comes from either the instrument and/or our measurement protocol. A possible explanation could lie in the difference in the sensibility of the detectors in the spectrophotometer. Concerning our measurement protocol, it should be noted that the exact quantity of powder used for each measurement was not perfectly weighted beforehand and a home-made sample holder had to be used, possibly leading to experimental mistakes. However, similar quantities of each powder were placed in the sample holder simply using visual reference for the filling. Using this protocol, small variations in the intensity of the optical response are observed for the repeated measure of the same sample but not to the extent of the 10+ fold shown between the hybrid and the pure oxides. In order to identify the origin of this supposed artifact in our spectra and confirm the observed tendencies, additional comparative measurements are being carried out on a different apparatus by the team of Prof. Aline Rougier (Dr. Issam Mjerji) at ICMCB – University of Bordeaux (France) as we write these lines.

h) Effects of an annealing treatment

The powders were annealed for one hour at 200°C and 500°C in both air and argon to study the effect of a thermal treatment on the atomic composition, the crystalline structure and the spectral behavior of the powder. Even though annealing is not required at this point in the work, it is a usual post-deposition treatment for wet coated films. Therefore, it was anticipated that it could be applied to our yet to be deposited films (cf. **Chapter 4**), hence the study of such a treatment on the properties of the powders. Another useful measurement to this purpose is thermogravimetric analysis (TGA). However, these measurements are still in progress as this Master Thesis is being completed. Pictures of the powders as well as X-ray diffraction and reflectance results are presented in *Figure 22* below.

Since all the hybrids present similar properties, only the annealing of $MoWO_x$ 1:1 is studied as a representative case for simplicity's sake.

First of all, we observed a significant modification in the coloration of the powders after the treatment at 500°C in open air. The powder went from dark blue to bright yellow. This yellowish color can be found in stoichiometric oxides such as WO_3[56]. This indicates that the oxygen vacancies initially present in the material are responsible for its pristine blue coloration and, if present in a sufficient concentration, for the plasmonic optical properties of the compound[41]. However, if the thermal process was carried out in an inert atmosphere, or if the temperature is kept lower than 200°C, the powders remain visually identical. The difference in results between annealing in air in comparison to annealing in an inert atmosphere also goes to show the central role of atmospheric oxygen during the thermal treatment.

Almost no variation in the crystallinity of the compound is observed up to 500°C in argon and in air. Only a slight shift of the peaks towards higher 2θ values can be noted in these extreme cases. This indicates a shrinking of the cell parameters that could result from partial or total oxidation of the material in argon and air respectively. The lack of equatorial oxygen in the crystal lattice could cause the structure to be looser. The insertion of oxygen back into the crystal would fill the previously vacant sites, shortening the bond length between oxygen and metallic atoms and tightening the structure, causing the shrinkage of the cell parameters and the corresponding shift in 2θ values according to Bragg's diffraction law.

However, annealing at 500°C in air results in the formation of stoichiometric $Mo_yW_{1-y}O_3$, with the complete passivation of the existing oxygen vacancies. When comparing the diffractograms of the powders at room temperature, annealed in air at 200°C and 500°C, the shift of the two peaks towards greater values is visible as the temperature goes up. This shows the transition from the more amorphous $MoWO_x$ to its stoichiometric oxidized phase, showing the responsibility of oxygen insertion in the displacement of the peaks.

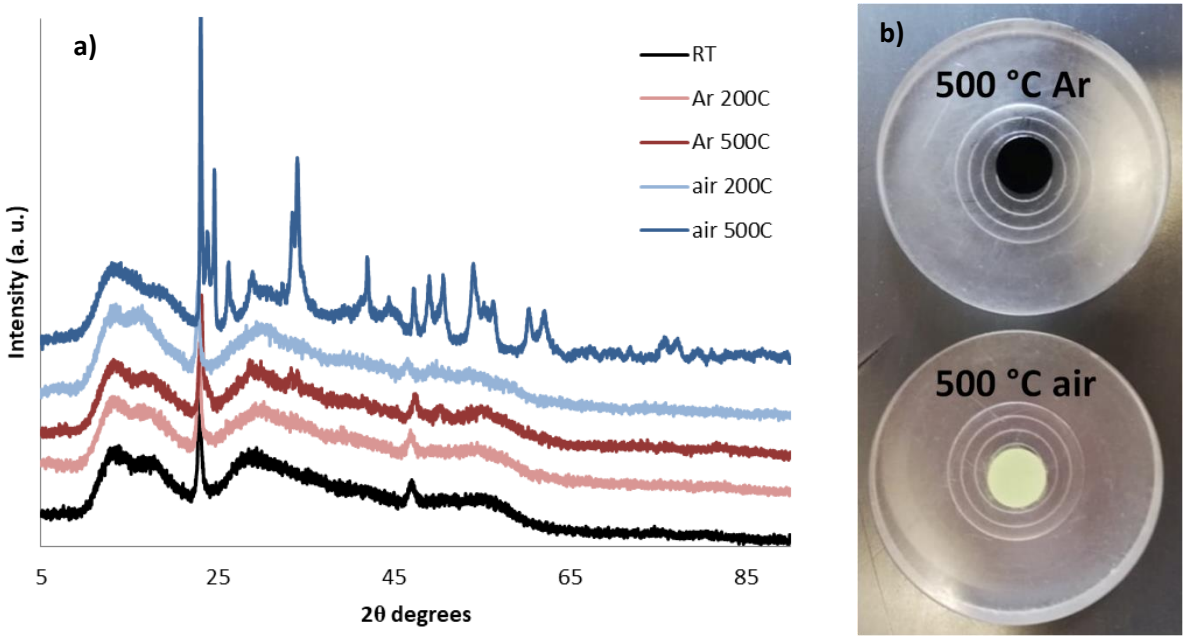

Figure 22: a) diffractograms of the $MoWO_x$ 1:1 powder at room temperature and after annealing at 200°C and 500°C in air or argon, b) pictures of the same powder after annealing at 500°C in air and argon.

Reflectance measurements of the annealed powders also showed tendencies related to the specific temperature and atmosphere used for the annealing treatment. Namely, moderate variations of the signal in the case of 200°C annealing in air and up to 500°C in argon while annealing at 500°C in air displayed major modification of the optical properties of the powders. The spectra of the powder at room temperature and annealed at 200°C in Ar are similar. Annealing at 200°C in air and 500°C in Ar result in a decrease in the intensity of the peak, losing around 20 % of its intensity. Even though the optical response of the material is impacted by the thermal treatment, the signal is conserved.

This behavior towards annealing tends to show that the optical response observed in the spectra is indeed plasmonic. The LSPR of the material depends on the concentration in free charge carriers. During the thermal treatment in air, the material is oxidized and the amount of free electrons available in the powder decreases until complete oxidation of the product is achieved. Since the oxidation of the material decreases the amount of free charge carriers, the intensity of the LSPR peak should decrease in return. This exact result can be seen in *Figure 23*, with the intensity of the peak decreasing at 200°C and disappearing when stoichiometric $MoWO_3$ is recovered from the annealing process. While this is not a straightforward evidence of it, the different reflectance measurements indicate the probable plasmonic character of the different MoWOx powders synthesized in this work.

In addition, these results indicate the opportunity of perfoming moderate annealing treatments of the materials, especially when processed as thin films (cf. Chapter 4) with no major alteration of its properties. However, when exposed to higher temperature in oxidative atmosphere (e.g. 500°C in air), the spectral response of the powder decreases

almost down to baseline level. In this case, the optical properties of the powder are lost, exhibiting the limitations one faces when it comes to thermal treatments of sample (as powder here and as film later in the manuscript) in order to improve morphology, stability (including adherence) or electronic and optical functionality.

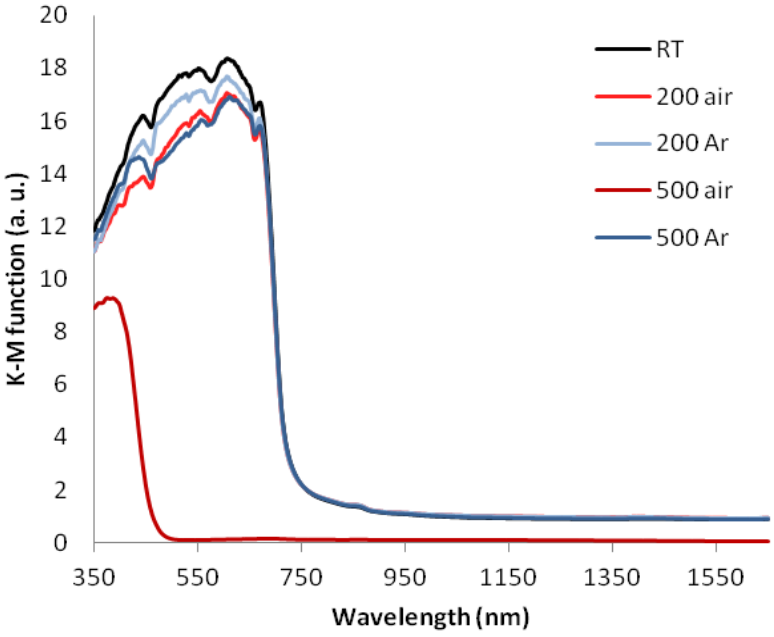

Figure 23: Absorbance spectra of the the $MoWO_x$ 1:1 powder after annealing at 200°C and 500°C in air or argon.

The synthesized powders displayed the expected morphologies, crystallinity and optical properties, in good correspondence with what was reported in the reference work of Yamashita et al. However, additional measurements using better controlled protocols are required before any conclusions are drawn from the optical spectra given their odd appearance.

Before these powders are used as "electrochromic inks" for the deposition of active films on conductive glass substrates (cf. **Chapter 4**), we studied their behavior in suspension and attempted to improve the stability of the latter by tuning different parameters such as the solvent, the pH or the addition of stabilizing agents (cf. **Chapter 3**).

Chapter 3 – Colloidal chemistry of MoWOx NCs: towards stable suspensions in polar, low-toxic media

After the characterization of the powders, we studied the dispersion of the nanocrystals in selected solvents for the formulation of "precursor inks" and their deposition as electrochromically-active films. For this purpose, we favor the use of common, low toxic solvents such as water and alcohols. If necessary, dispersing agents are added to improve the stability of the suspension.

We base our choice of dispersants on their ability to improve the stability of the suspension and their beneficial effect on the properties of the active layer in the context of electrochromic device (cf. discussion of the case of polyethylene glycol below). If their residual presence in the films is detrimental to their functionality, the dispersing agents should be easily eliminated by the mean of soft thermal post-treatment.

3.1. Dispersant-free suspensions

First, pristine dispersions are prepared from the different powders synthesized previously (cf. **Chapter 2**), meaning Mo_{3-x}, WO_{3-x} and $MoWO_x$ 1:1, 2:1 and 1:2. Various usual, polar and low-toxic solvents (ethanol, isopropanol, water) are considered, and attempts to disperse the as-synthesized powders are performed according to a standard protocol[57]: powders are weighed and mixed with a precise volume of solvent using concentrations from 0.5 to 10 g/mL. The dispersions are magnetically stirred for 30 min, and then treated using an ultrasound probe to break the aggregates. Forty pulses of 0.5 s each are applied after which the suspension is placed back on the magnetic stirrer for further agitation overnight. However, based on visual assessment, none of the suspensions were stable for more than a few minutes at best (*Figure 24*).

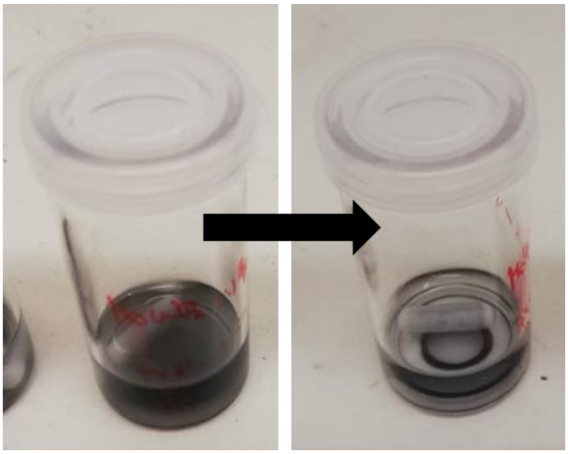

Figure 24: Evolution of a dispersion of $MoWO_x$ 1:1 as a function of time with the original suspension (left) and the same suspension a few minutes later (right).

In order to obtain more quantitative insight on the dispersions colloidal behavior and (in)stability, zeta potential measurements, quantifying of the surface charge of solid particles in suspension, are performed while varying different parameters. If the acquired value for the surface potential of the material is greater than |20| mV, the suspension is usually considered stable. Zeta potential measurements a carried over on a DT-1200 electroacoustic spectrometer in order to study the stability of 1 %wt. suspension of each powder (≈10 mg/ml) and its evolution with the modification of the pH.

From the results shown in *Table 3* below for suspensions in ethanol, the first observation is the difference in the values obtained for the pure oxides – respectively -31 and -14 mV for MoO3-x and WO3-x – in comparison with the hybrids – respectively +3, +4 and +9 mV for MoWOx 2:1, 1:1 and 1:2. The zeta potential values of $MoWO_x$ 1:1 and 2:1 are thus similar while the potential of $MoWO_x$ 12 differ significantly. Even though $MoWO_x$ 1:2 differs from the two other hybrids mainly because of the presence of excessive WO_{3-x}, it is unlikely that this excess is responsible for the increase in the zeta potential given the very negative zeta potential of WO_{3-x} (*Table 3*). Even though the zeta potential value differs from one ratio to the other, the potential is not high enough for the suspensions to be considered stable.

Compound	Zeta potential (mV) in EtOH
MoO_{3-x}	-31
$MoWO_x$ 21	+3
$MoWO_x$ 21	+4
$MoWO_x$ 21	+9
WO_{3-x}	-14

Table 3: Zeta potential measurements for suspensions of each powder in ethanol.

The stability of the suspensions in water is also investigated. In this case, we only studied $MoWO_x$ 1:1 as a representative case because of time and material limitations in the frame of this work. Using water as a media allowed us to study the influence of the pH on the stability of the suspension. Aqueous suspensions are assessed in terms of zeta potential evolution as the pH varies. The pH is adjusted by addition of NH_4OH 0.1 M to roughly cover a range starting at 2 up to 9. The results are shown in *Figure 25*.

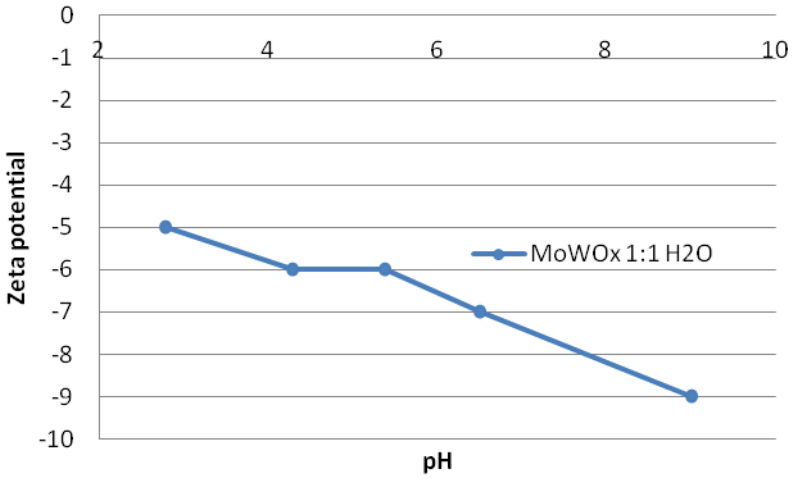

Figure 25: Evolution of the zeta potential of $MoWO_x$ 1:1 in water as a function of pH.

As the pH increases, the overall result on the zeta potential of the powder is a decrease in the measured value, starting from -5 mV and decreasing down to -9 mV in moderately basic conditions (pH = 8-9). This increase in the absolute value of the zeta potential seems to indicate a relative increase in stability. This improved stability probably arises from the deprotonation of acidic sites at the surface of the material in basic media. Positive charges will appear on the solid as a result from this acid-base reaction, repulsing each other and therefore increasing the overall stability of the suspension.

Another useful property for the development of stable suspensions in aqueous solvent is the point of zero charge (PZC). The PZC is the condition at which the negative and positive surface charge densities of a material are equivalent, making the overall charge equals to zero. For most solids, the PZC is strongly pH dependent and its determination takes place by the titration of a suspension of the material of interest.

Here, we adapted a previously published method by Bertus et al.[58] in which a suspension of the hybrid in the weak base NH_4OH 0.1 M is titrated with HCl 0.1 M.

The resulting titration curve and its first derivative are presented in *Figure 26.a* and *b*. Two distinct drops are visible in the titration curve. The first one could correspond to the acid-base reaction between soluble species formed in an alkali media and the acid while the second one is the actual titration of the active surface sites of the powder. Such behavior has already been shown in the same publication from Bertus et al. in the case of WO_3 NCs in the presence of NaOH, forming Na_2WO_4 further dissociating into soluble WO_4^{2-} species[58]. Therefore, the neutralization of these soluble species takes place at the first drop and only the second one is considered in the estimation of the PZC.

To determine the exact point of inflection of the curve, its first derivative was computed. The apex of the second peak corresponds to the reaction with the active surface sites. At this point, the concentrations in protonated and deprotonated sites are equal and the overall charge of the material equals zero. This point can be correlated with a volume of titrant. For the same volume in the first titration graph, the corresponding pH value is the PZC of the powder. For $MoWO_x$ 11 (representative case), a PZC value of 4.4 is found (*Figure 26*).

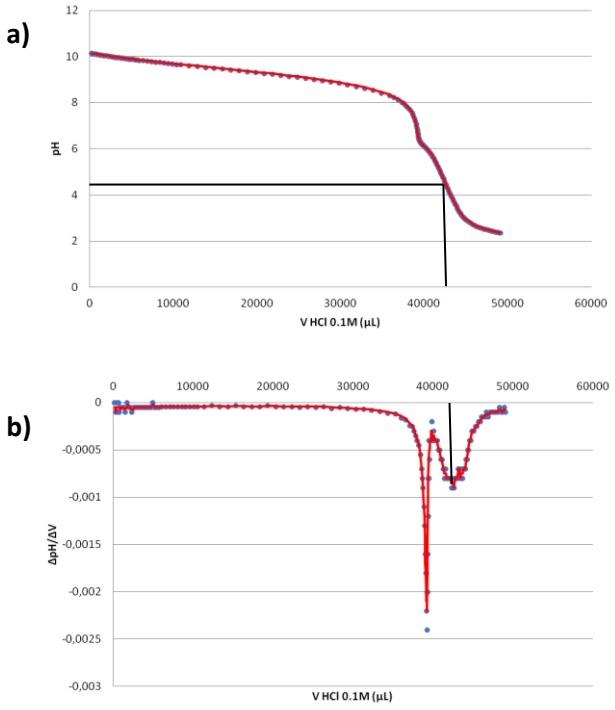

Figure 26: a) titration curve of a $MoWO_x$ 1:1 suspension in aqueous media and its first derivative (b).

The instability of the bare hybrid suspensions in water and ethanol could be determined from both qualitative and quantitative assessment. We observed a slight increase in the zeta potential of aqueous suspensions in alkali pH but the values are still insufficient to be considered stable (zeta potential ≥ |20| mV). Therefore, the use of dispersive agents was considered.

3.2. Dispersant-containing suspensions

In a second time, specific surfactants are added in different concentrations in order to improve the dispersions stability as a function of time and surfactant/NCs weight ratio. Concretely, polyethylene glycol (PEG 140k), Triton X100 and polyvinylpyrrolidone (PVP) are added (separately) to suspensions in ethanol for weight percentages going from 20 %wt. to 1000 %wt. of the hybrid powder content. On the other hand, polyethyleneimine (PEI) is used in aqueous suspensions with a 5%wt. concentration.

The stabilization of the suspensions following the addition of these agents can arise from multiple processes depending on their class: steric, electrostatic or electrosteric materials. Steric materials stabilize the suspension by increasing the steric hindrance between the particles, preventing them from aggregating and precipitating. On the other hand, electrostatic dispersants possess chemical functions that can be charged by protonation/deprotonation depending on the pH. These charged moieties act on the surface properties of the suspended solid, impacting the surface charge to improve the repulsions between particles and once again prevent their precipitation. Lastly, electrosteric agents combine the effects of both electrostatic and steric stabilization, filling the space between particles and modifying their surface properties. These mechanisms are shown in *Figure 27* below.

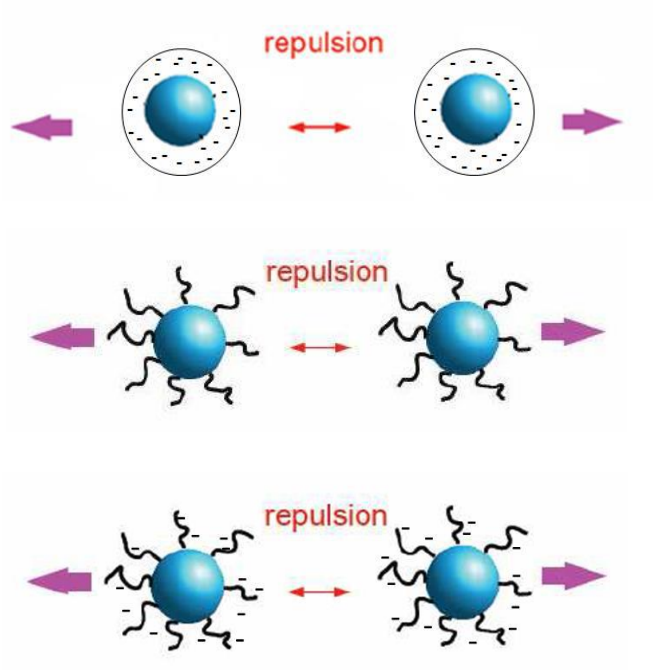

Figure 27: Stabilization mechanisms of solid suspensions in liquid media: a) electrostatic repulsion, b) steric repulsion and c) electrosteric repulsion[59].

The choice of the different surfactants is mainly driven by a preliminary literature review[60-62] and by the XRD and reflectance results obtained after powder annealing (cf. *Section 2.1.h*): the powder can be thermally treated up to 200°C with no significant loss of its optical activity and conservation of the crystal structure responsible for the plasmonic properties of the material. On the other hand, some surfactant may have a beneficial effect on the functionality and/or efficiency of the film-deposited material and would not require to be removed from the layer. Ethylene oxide-based surfactants such as PEG are an example of potentially-beneficial additives in view of their strong affinity towards Li^+ ions, which can positively impact the electrochromic mechanisms inside the films (cf. *Section 1.2.b*).

However, after multiple trial-and-error tests, addition of the different surfactants showed little improvement in the stability of the suspension, not holding for more than 30 minutes before strong precipitation could be observed. The best results were obtained with 20% PEG in ethanol and 5% PEI in water, respectively (*Figure 28*). In the aqueous solvent, the solution has a cloudy appearance and the addition of the surfactant lead to increased stability over a 10 minutes period (based on visual observations of the resting suspensions over time). However, assessment of its effect on the electrochromic properties of the final film is required since PEI elimination temperature is ~250°C. At this temperature, the oxidation of the hybrid material will take place and the vacancies are gradually filled, decreasing the concentration in free charge carriers and thus the optical intensity of the plasmon. If the additive presents a detrimental effect to the electrochromic response of the film, its degradation at such high temperature will further impede the good efficiency of the material because of the decrease in available free electrons.

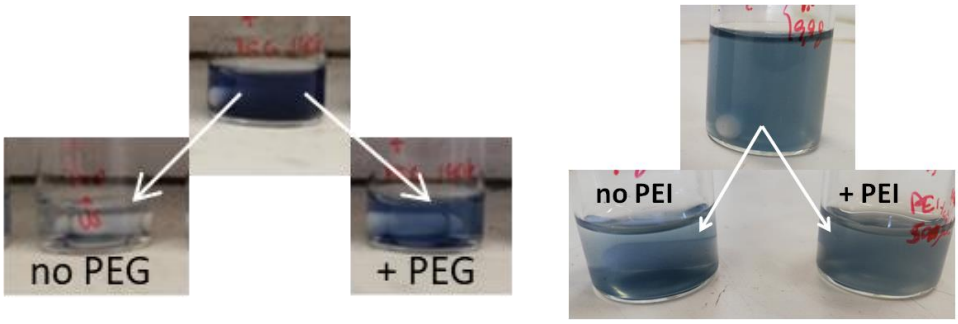

Figure 28: Pictures of the stabilized-suspensions over time: a) $MoWO_x$ 1:1 + PEG 140k 20%wt in ethanol and b) $MoWO_x$ 1:1 + PEI in water.

To better understand the stabilization process of our suspensions, quantitative measurements were carried out on the dispersant-stabilized suspensions using zeta potential. First, we studied the behavior of the potential of each powder when a surfactant was progressively added to the suspension. The resulting graph can be found in *Figure 29.a.* Increasing the PEG concentration in EtOH dispersions (representative case of MoWOx 1:1) show no effect on the stability of the suspension. This effect is explained by the nature of the additive: PEG is a purely steric agent, the stability brought by this compound lies in its ability to occupy the space between the particles and prevents them from agglomeration and ensuing precipitation.

Meanwhile, the addition of PEI in aqueous dispersions of the different MoWOx NCs induces a shift of the zeta potential from +3-4 towards ~+7-9 mV (*Figure 29.b*). PEI is an electrosteric stabilizer, acting both on the steric hindrance between the particles but also modifying their surface properties. Indeed, PEI is a polymer of ethyleneimine with –NH functions that can be protonated in acidic media. Therefore, the charged chain can interact with the particles and impact their surface charge.

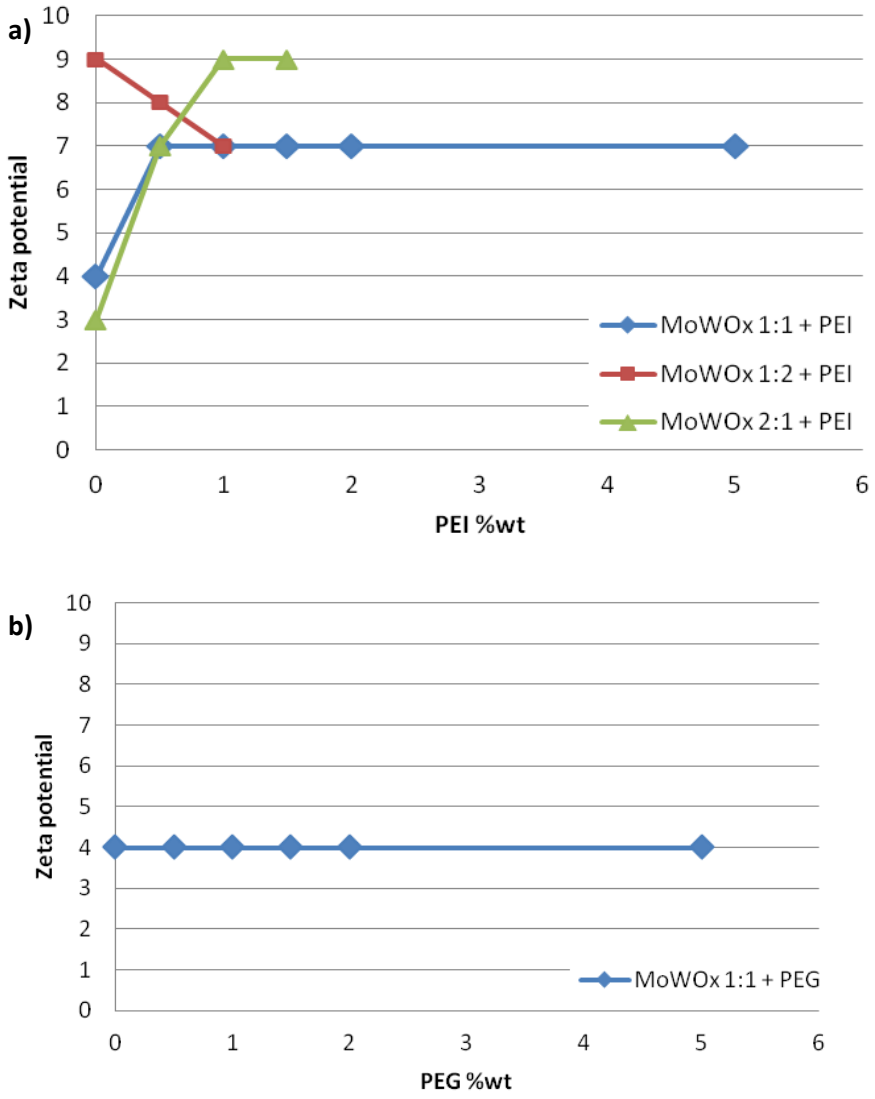

Figure 29: Evolution of zeta potential values of the hybrids as a function of the weight content in dispersing agent: a) $MoWO_x$ 1:1, 1:2 and 2:1 in water + PEI, b) $MoWO_x$ 1:1 in ethanol + PEG 140k.

Preliminary assessment of the effect of usual solvents and dispersing agents on the stability of the NCs suspensions highlights the interest of dispersant-stabilized suspensions. The best results for 1%wt. oxide suspensions were obtained with the addition of 20%wt. PEG 140k in ethanol and 5%wt. PEI in water (at basic pH values). Nevertheless, the use of PEI as a dispersing agent is ruled out for now due to its degradation temperature. The latter, at 250°C, is too high and the stabilizing agent cannot be eliminated from the active material by thermal treatment without affecting the optical properties of the layer. Therefore, only suspensions of PEG 140k in ethanol were considered for the deposition of active films in **Chapter 4**.

Chapter 4 – Thin film processing of $MoWO_x$ NCs and primary assessment of their electrochromic behavior

Now that the product of interest could be synthesized and dispersed into handleable "inks", we consider its deposition onto glass substrates as individual working electrode component of an electrochromic device.

Strategically, we focus on atmospheric-pressure wet deposition methods such as spray coating, spin coating and blade / bar casting. In addition to the cost effectiveness of these methods in comparison with vacuum technologies, they can be easily implemented at a laboratory scale, but also at an upper, industrial scale in the case of spray and bar casting, which are compatible with roll-to-roll production processes. However, since this work represents only the exploratory steps in the development of novel electrochromic materials (both from a material and device standpoint), we chose to primarily use the more time-efficient spin coating and bar casting techniques. These methods do not require a too high level of dispersion stability because the deposition is quasi-instantaneous. This allows us to work with suspensions displaying relatively low stability in comparison with other deposition methods such as spray coating for example (for which the engaged volumes are quantitatively more important).

4.1. Wet coating methodologies

a) *Spin coating*

Spin coating is usually performed as follows: first, the substrate is placed in the apparatus and held in place thanks to a continuous vacuum at the base of the support. Then, the solution or suspension is deposited onto the substrate. In the next step, the rotation of the whole sample causes the liquid to cover the whole surface of the substrate. During this step, the extra solution/suspension is expelled off the substrate because of the applied centripetal force. Finally, the film is dried in ambient air or by a thermal treatment depending on the materials, the solvent and the speed of evaporation[63].

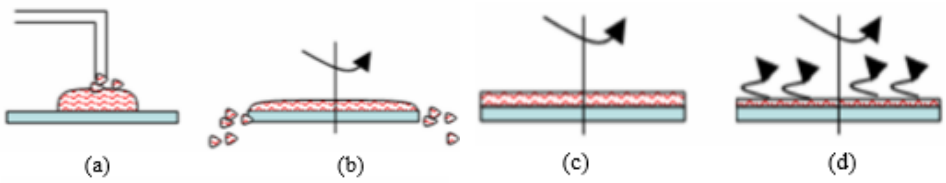

Figure 30: Schematic representation of the spin coating process: a) deposition of the suspension, b and c) rotation spreads the liquid on the surface of the substrate, the excess is ejected from the surface, d) the rotation slows down and the solvent is evaporated.

b) Bar / blade casting

The bar / blade casting approaches involves the use of a frame so to spread a thick suspension onto a substrate. Before the deposition takes place, the suspension is placed in the reservoir of the frame. One side of the frame is the actual blade / bar, placed at a short distance from the surface of the substrate that will define the thickness of the deposited layer. Once the frame moves across the deposition area, some of the suspension is allowed to flow through the space left between the bar / blade and the substrate, spreading onto the surface and forming a film. The morphology and thickness of the films can be modified by adjusting various parameters, notably the distance between the bar / blade, the speed of the frame in relation to the surface, the temperature of the surface and the nature of suspension (viscosity, concentration …)[64].

Bar coating experiments are conducted in collaboration with the team of Prof. Aline Rougier and Dr. Issam Mjerji at ICMCB – University of Bordeaux (France).

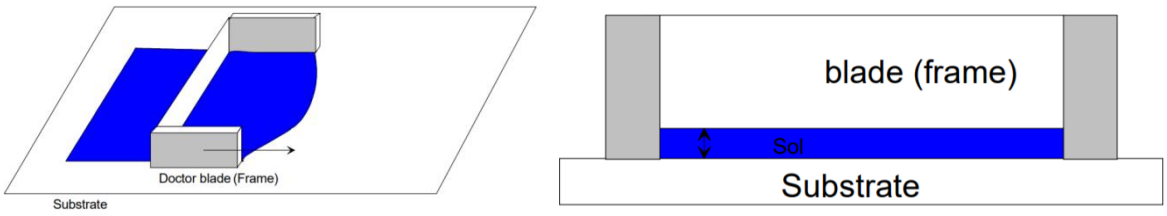

Figure 31: a) schematic representation of the bar casting process, b) side cut of the frame showing the space between the blade/bar and the substrate[64].

4.2. Thin film processing of $MoWO_x$ NCs by spin coating

Due to limitations of materials and time, only the MoWOx 1:1 case could be studied in the framework of this work. The dispersion protocol has been discussed in Chapter 3. As a brief reminder, dispersions of 10 mg/mL concentration, eventually containing PEG 140k in a 20% weight ratio, are magnetically stirred for 30 min, treated using an ultrasound probe and placed back on the magnetic stirrer for further agitation overnight.

The prepared inks are further spin-coated onto FTO-glass substrates (PG-Fast 15 ohms/square, 2.0 x 2.0 x 0.4 cm) using a SCS P-6708D spin coater. The glass substrates are preliminary rinced with acetone and ethanol before being blown dry and further treated by UV-ozone for 20 minutes before the deposition. A piece of FTO-coated glass is placed on the spin support and dispersion is spread over the surface before the rotation begins (stationary deposition method). The sample is rotated at 1000 rpm for 1 second, followed by consecutive 5 seconds at 1200 rpm and 5 seconds at 1500 rpm. Multiple layers of the material are deposited, each consisting in 50 µL of suspension (an appropriate amount for a tradeoff between the complete coverage of the surface and a minimal waste of suspension

during the deposition process). After completing the deposition of the desired number of layers, the substrates stabilized using a mild thermal treatment at 100°C for 10 minutes.

The visual homogeneity of the films highly depends on the deposition parameters and the preparation of the suspension. In the case of the spin, the obtained films, prepared from 10 mg/mL dispersions, are not very uniform, displaying a quite characteristic deposition pattern of spin coating, with a concentric spot in the middle of the substrate where the centripetal force is the weakest and line going outwards starting from this central spot (*Figure 32.a*, even if the mentioned lines are not very visible on the picture). In addition, the films suffer from fairly poor adherence, being stripped off of the substrate at a simple touch or when rinsed with a solvent (this is clearly visible in the lower section of *Figure 32.a* where a finger trace can be observed as the film was removed).

Given the poor properties of this film, we further considered a similar suspension in which PEG 140 k was added in an attempt to improve the stability of the suspension and therefore the global quality of the deposition. Using this method, we obtained films with higher mechanical adherence, not anymore affected by touching or even scraping with the tip of a metallic pincers. However, the formation of PEG polymeric aggregates in the precursor dispersions yields very inhomogeneous films exhibiting a mottled appearance visible in *Figure 32.b*. This agglomeration can be lowered by heating the suspensions at 60-70°C for a few minutes prior to the deposition, visually leading to more homogeneity and dispersity. The films deposited after using this thermal treatment are more uniform and adhere to the surface. However, the layer of deposited material seems to be thinner than in the previous case (*Figure 32.c*).

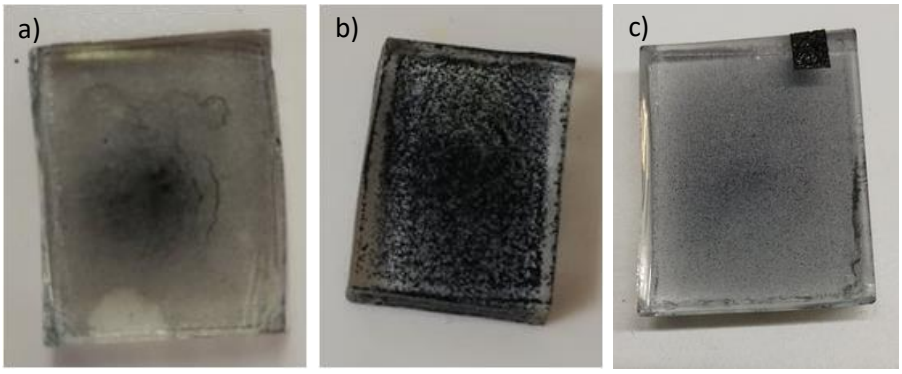

Figure 32: Pictures of the spin coated films showing the appearance of the deposited film: a) $MoWO_x$ 1:1, b) $MoWO_x$ 1:1 + PEG 140k 20%wt., c) $MoWO_x$ 1:1 + PEG 140k 20%wt. heated.

Given the unusable character of the films produced by spin coating without the addition of a surfactant they were not studied any further. Furthermore, as previously mentioned in *Section 3.2*, PEG as polyethylene oxide material can bring a positive additional impact regarding the electrochromic properties of the film in view of its strong affinity with lithium

ions, making it an interesting case of low-cost and efficient polymer electrolyte species[65]. This could potentially induce a more important penetration of ions deeper into the active layer and improve the overall efficiency of the device by increasing the effective area of the material. However, PEG may act as a double edged sword: if the affinity between PEG and Li^+ is too strong, the lithium ions could be trapped inside the electrochromic material, permanently activating some of the sites and leading to less available active sites, decreasing the contrast between the colored and bleached states. Therefore, if the surfactant content is too high, the material might even become unusable, blocked in a permanent colored state.

The morphology of spin coated films with PEG, heated or not prior to the deposition, is presented in the following micrographs. Heating the suspension clearly leads to more homogeneity of the deposition. However, the coverage of the surface might be similar in both cases. Indeed, even if the film produced with the heated suspension is more homogenous, there is no continuous layer of material on the surface of the substrate. In the untreated suspension, the inhomogeneously dispersed spots actually form a localized fully covering film over the FTO layer. This greater covering of the surface can be seen at higher magnification (*Figure 33* – representative case of MoWOx 1:1).

a)

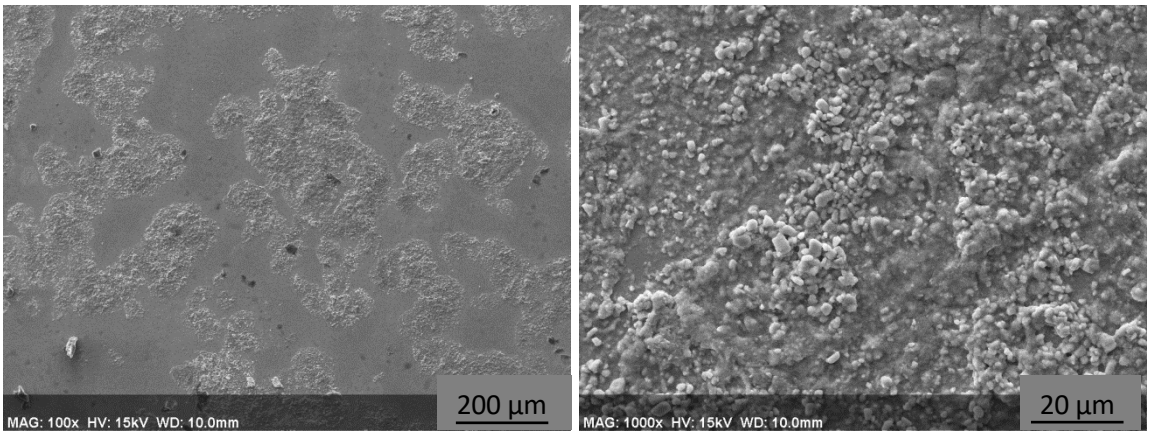

b)

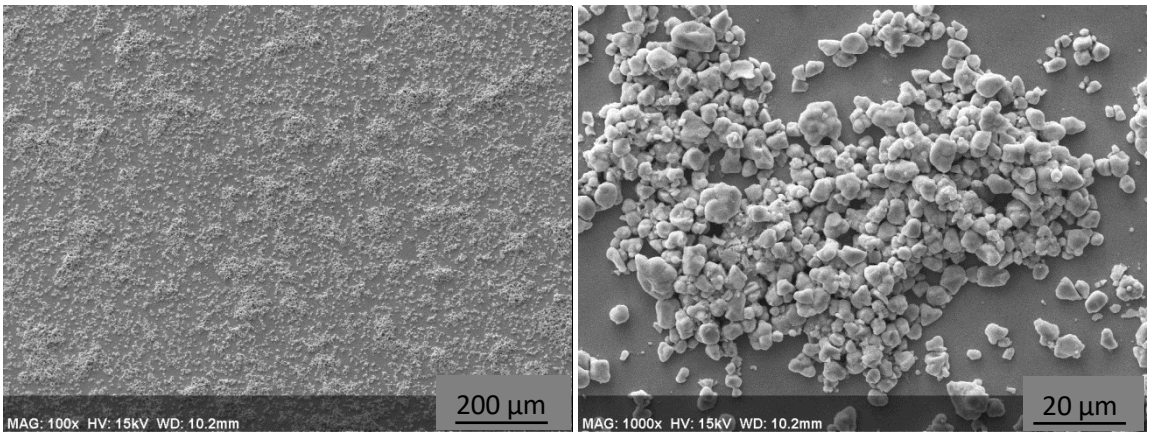

Figure 33: SEM micrographs of the spin coated films: a) $MoWO_x$ 1:1 + PEG 140k 20%wt., b) $MoWO_x$ 1:1 + PEG 140k 20%wt. heated and respective magnifications.

4.3. Thin film processing of $MoWO_x$ NCs by bar coating

Regarding bar coating, the deposition of molybdenum-tungsten oxide NCs was made using a RK K Control Coater. Due to materials and time restrictions, only the MoO3-x and $MoWO_x$ 2:1 cases could be fully studied in the framework of this work. A highly-loaded suspension (~150 mg/mL) is spread here onto conductive FTO glass substrates using the bar coater apparatus. The suspensions used for bar casting are far more concentrated, in a trial to improve the stability of the suspension by optimization of the steric hindrance between the particles. In addition, the high solid content of the suspension increases the viscosity to meet the requirements of the bar coating deposition method. In comparison, the concentrations used for the spin should be far lower for the suspension to be liquid enough and easily spread on the substrate, therefore yielding uniform deposition over the whole surface of the sample. Using bar coating, we obtained films displaying superior adherence and homogeneity in comparison to spin coating all without any requirement for the use of surfactant or post deposition treatments (*Figure 34*).

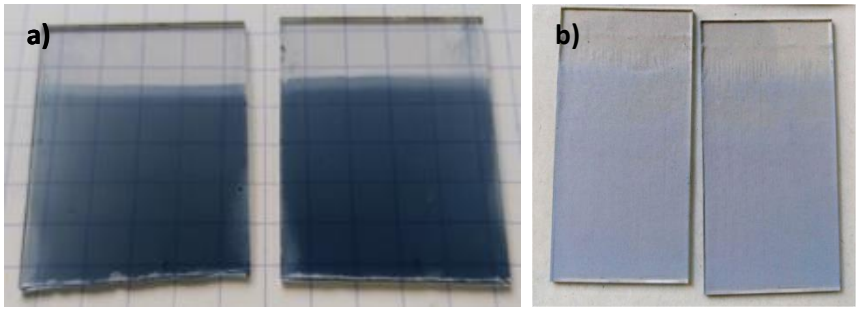

Figure 34: Pictures of the bar casted films showing the appearance of the deposited film: a) $MoWO_x$ 2:1, b) MoO_{3-x}.

The blade coating technique yielded several exploitable samples; the micrographs corresponding to the best films are displayed in *Figure 35*.

On the first hand, the bar coating of $MoWO_x$ 21 produces highly homogenous and thick (1-2 µm) films. The surface is fully covered by a layer of material and not only by the bigger particles (as seen in the magnified insert in *Figure 35.b*). Therefore, this film has a combination of both superior homogeneity, surface coverage and sufficient adherence in comparison with all the spin trials. On the other hand, the deposition of suspended pure MoO_{3-x} gave results similar to what was observed by spin-coating with the heated $MoWO_x$ 1:1 + PEG dispersion (cf. *Figure 32.b* above). The particles are organized into large aggregates uniformly distributed on the surface but not as a continuous layer between and below the larger particles. Therefore, in the case of $MoWO_x$ 2:1 films, it could be deduced than the said continuous layer is constituted of a more important quantity of dispersed, individual $MoWO_x$ nanorods instead of uniquely large aggregates as those that were previously observed in the micrographs of the powders in *Section 2.1.d*, *Figure 17*.

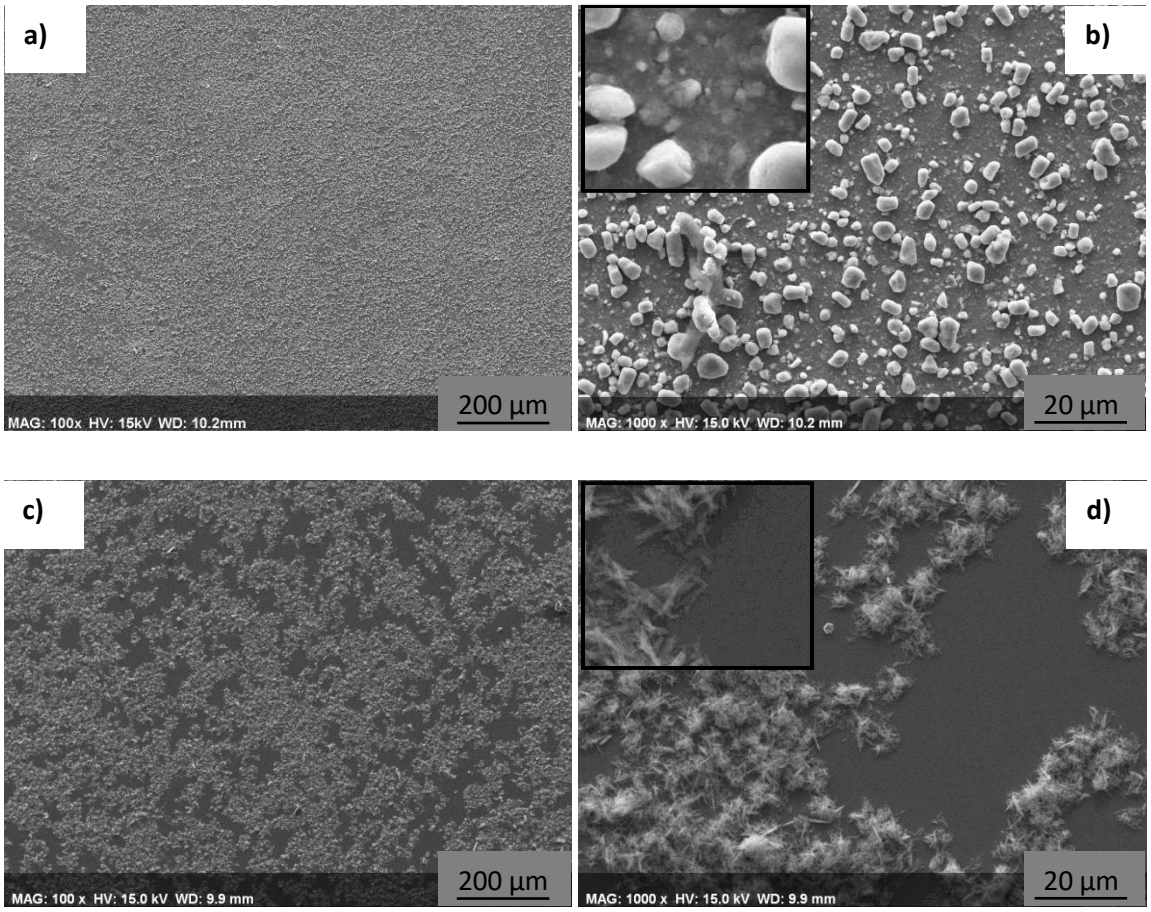

Figure 35: SEM micrographs of the bar coated films: a) $MoWO_x$ 2:1and b) same film at a greater magnification, with a close-up of the surface in inset, c and d) MoO_{3-x} film, magnified image of the film and close-up of the surface in inset.

4.4. Electrochromism of $MoWO_x$ NCs films: preliminary trials

The electrochemical properties of the "optimal" films highlighted beforehand were investigated using a Biologic SP200 Potentiostat. The films were measured in a half cell configuration (cf. *Figure 36*). This setup consists in an "open cell" in which the film is immersed in a liquid electrolyte consisting in a mix of lithium bis(trifluoromethanesulfonyl)imide and 1-ethyl-3-methylimidazolium-TFSI (LiTSFI-EMITFSI ionic liquid)), a reference electrode (saturated calomel electrode, SCE) and a platinum counter electrode.

During such preliminary testing of the films, the "proof-of-concept" of the electrochromic character of the various molybdenum-tungsten oxide-based electrochromic films could be established (or not) by observing (or not) a reversible coloration / bleaching behavior of the films in reaction to consecutive negative and positive bias of the working electrode, either in cyclovoltammetric or potentiostatic (chronoamperometric) mode (see below).

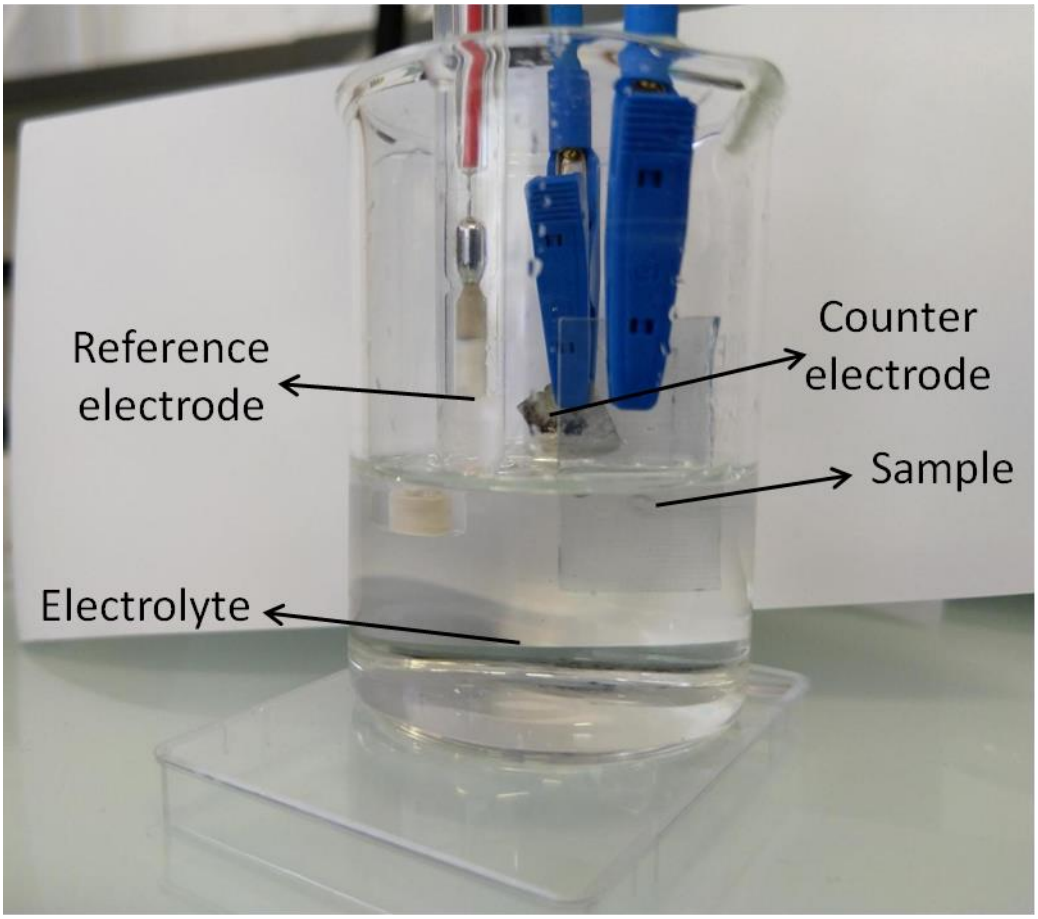

Figure 36: Experimental setup for qualitative and quantitative assessment of the electrochromic properties of the films.

a) Cyclic voltammetry (CV) measurements

A global investigation of the electrochemical behavior of the different films are first carried out by CV measurements, with the recording of current cycles upon potential bias from open circuit potential within a potential window comprised between -1 and +1 V vs. SCE at a 20 mv/s scan rate. In good accordance with W and Mo redox behavior (cf. Chapter 1), the films are first colored by the application of the negative potential, then bleached back by reversing the bias towards positive potential values. It should be noted that in the context of this work and due to materials and time limitations, we chose to avoid the discussion of the different sorts of active layers comparatively to each other: the conditions of films preparation are indeed too different from one sample to another (e.g. spin-coated films vs. bar-coated ones) and imply too strong differences in terms of layers thickness, structure and density, all impacting the exact nature and intensity of the charge transfers between the electrode and the electrolyte.

The cyclovoltammetric curves measured on spin-coated $MoWO_x$ 1:1, bar-coated $MoWO_x$ 2:1 and MoO_{3-x} films are respectively shown in *Figure 37.a*, *b* and *c*, with both first and tenth cycles being presented. For the sake of comparison, the CV curves recorded on a "reference"

stoichiometric WO3 film prepared from ultrasonic spray coating according to a well-established GREENMAT protocol[11] is shown in *Figure 37.d*. These films are known to exhibit great electrochromic properties such as 89% of transmission contrast at 550 nm and a close to 100% cycling reversibility over ~500 cycles.

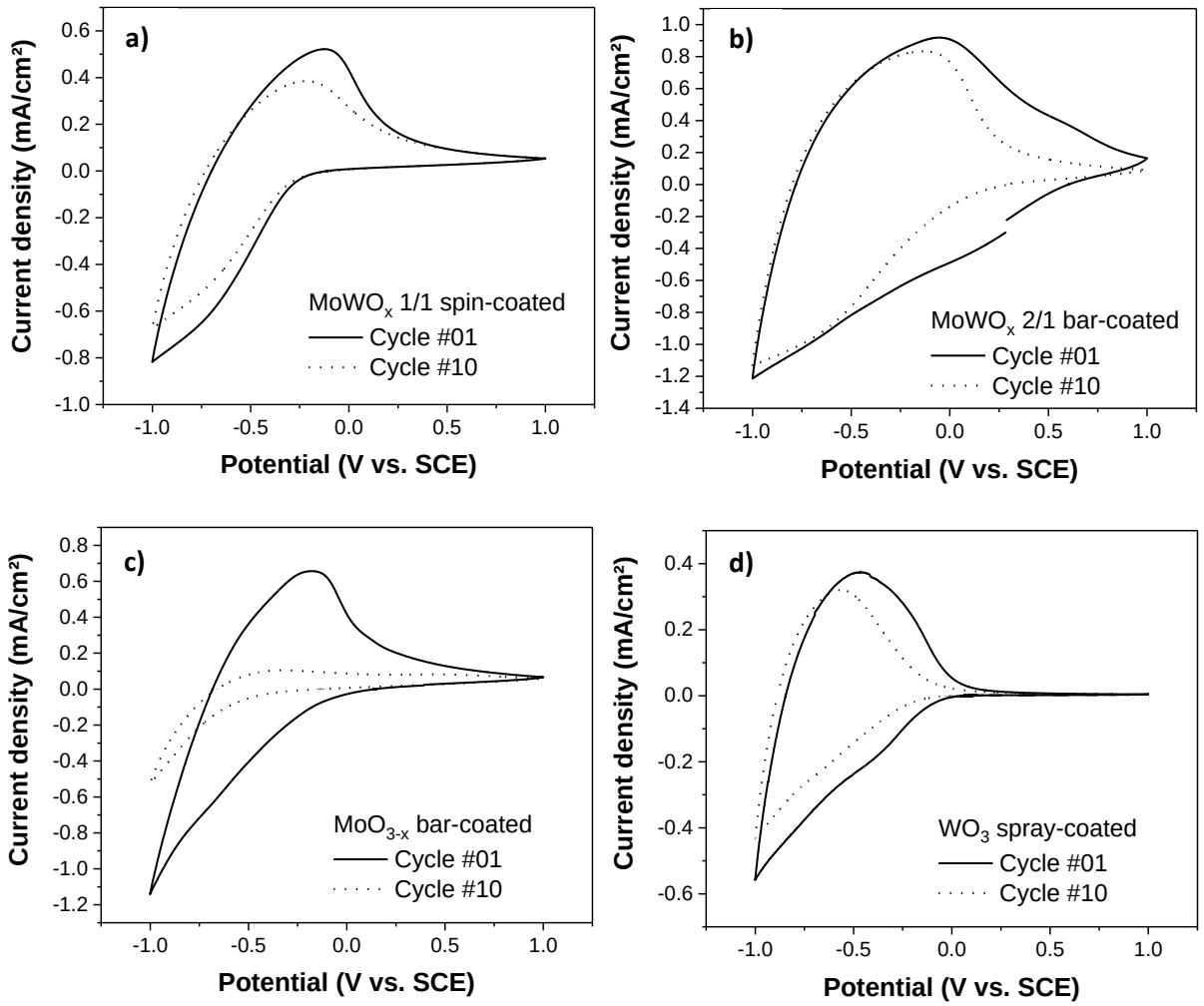

Figure 37: CV curves of the active films: a) spin coated $MoWO_x$ 1:1, b) bar coated $MoWO_x$ 2:1, c) bar coated MoO_{3-x} and d) spray coated WO_3 smartspray.

In all cases, a reduction wave is observed upon negative cycling followed by a broad oxidation peak upon positive cycling. The potential value corresponding to the maximal current value corresponds to a potential of ~-0.5 V for the WO3 sprayed films while being centered at -0.1 V for the MoO3-x film but also for the two MoWOx cases, the spin-coated 1:1 and the bar-coated 2:1. The last observation seems to indicate that MoWOx films studied here are more governed by the redox reactivity of the Mo atoms rather than the W ones.

Another observation to be made is the relative cycling instability of the MoO3-x film, showing a loss of ~80% of its initial current value only after 10 charge/discharge cycles, while the two sorts of MoWOx films remain quite stable over a large portion of the potential window. Indeed, if the CV globally retains its shape and intensity from one cycle to the other, the reversibility of the process is good, the amount of charge injected in the material is kept similar, meaning that most of the charges are also extracted during the application of an opposite potential. A good example of a durable device is displayed in the CV curve of the reference WO_3 sprayed film reference, where the current (and charge) remains consistent over consecutive charging (up to 500 cycles) with most of the charges being reversibly injected and removed from the material cycle after cycle (~100%)[11].

This particularity observed for our MoWOx layers may be the indication of a more durable capacitive behavior (more stable over cycling) brought by the combination of tungsten and molybdenum ions inside the crystalline structures generated here, as already observed in selected articles in literature[49]. Explications may be found in the respective redox behaviors of both elements: Mo can be reduced from Mo^{6+} to Mo^{5+} first and then further reduced into Mo^{4+}, with a total of 2 electrons exchanged, while W can mostly be reduced from W^{6+} to W^{5+}. Because of this additional reduction ability of the Mo ions, one can expect more charge to be stored in the films containing more molybdenum[49]. Regarding the MoO_{3-x} films, the poor cyclability and low reversibility of the charge exchanges may also be the indication of a detrimental trend of ions trapping in active sites, progressively inducing a drop of the absolute quantity of exchanged charges. This lack of reversibility and consecutive residual ion trapping will be confirmed further by observing the “non-bleached” aspect of the MoO3-x films (see below). Obviously, long-term cycling studies (over a minimum of 500 cycles) should be performed in other to confirm (or not) such trends.

b) <u>Potentiostatic runs and visual assessment of the electrochromic behavior</u>

In a further step, in order to observe the maximal amplitude of coloration/bleaching contrast, the different films are potentiostatically biased at -1.0 V and +1.0 V (respectively) for 1 min each. An ideal electrochromic behavior would be to get a fully reversible optical modulation with strong contrasts, as observed in the reference case of a sprayed WO_3 film (presented in *Figure 38* with, from left to right, the as-deposited state at open circuit voltage, the colored state at -1 V vs. SCE and the bleached state at +1 V vs. SCE)).

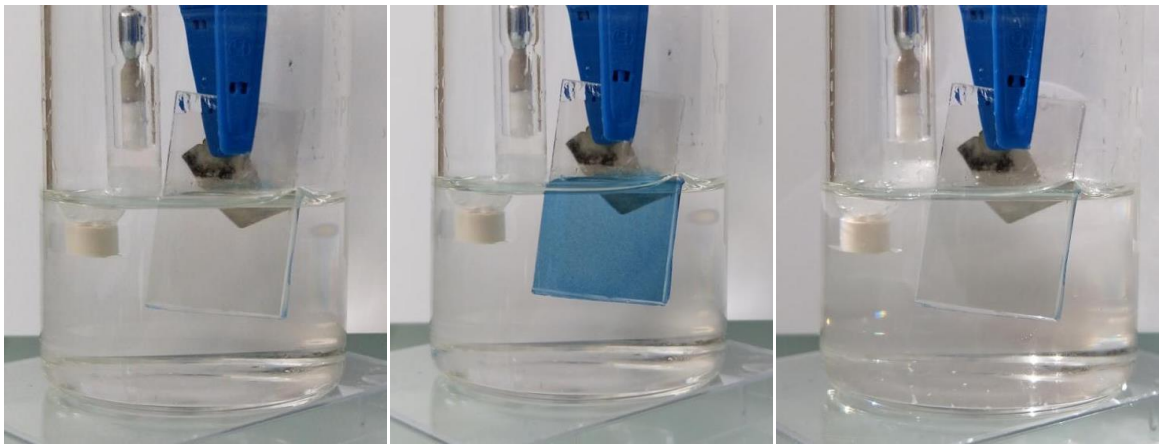

Figure 38: WO_3 "SMARTSPRAY" film in the a) as-deposited, b) colored, c) bleached states.

The spin-coated films prepared from not-heated PEG-containing dispersions of $MoWO_x$ 1:1 NCs (*Figure 39*) displayed an observable modulation in the visible range.

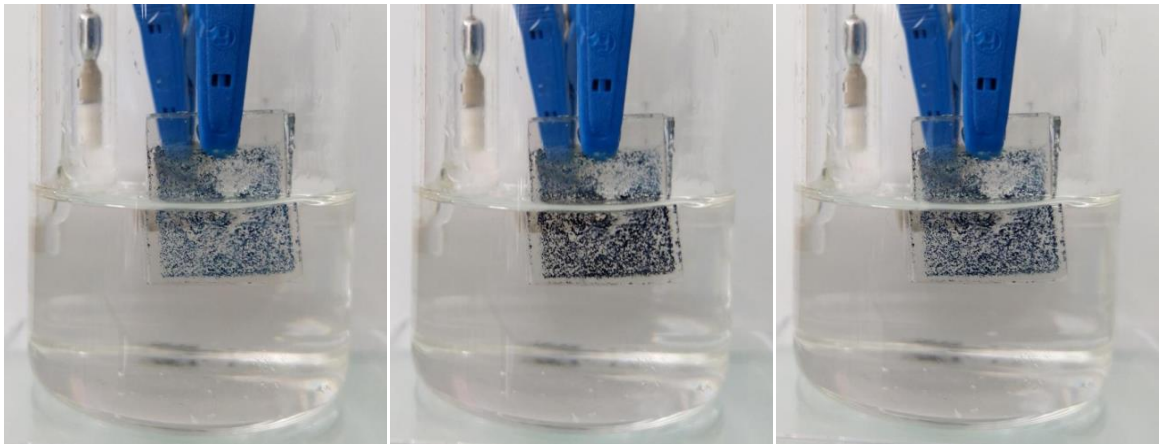

Figure 39: Spin coated $MoWO_x$ 1:1 film in the a) as-deposited, b) colored, c) bleached states.

The films can thus be colored in a darker blue shade as the potential decreases. However, when the oxidative positive potential is reversely applied, a slight bleaching of the samples is observed but not in a fully reversible way. Primarily, this irreversibility in the coloration process might be explained by the inhomogeneity of the samples or from the presence of residual PEG in the active layer (its detrimental effect upon Li+ trapping has been discussed in *Section 3.2*). However, when another film from the same batch was "mildly" annealed at 250°C in air for 1h and then submitted to the same potentiostatic run, the same "non-bleaching" behavior is observed (*Figure 40*), proving that to the thermal removal of the PEG incorporated in the layer cannot positively improve that aspect. From these observations, one can conclude that such annealing treatment of the sample displays neither detrimental effect nor improvement of the coloration/decoloration of the electrochromically-active layer.

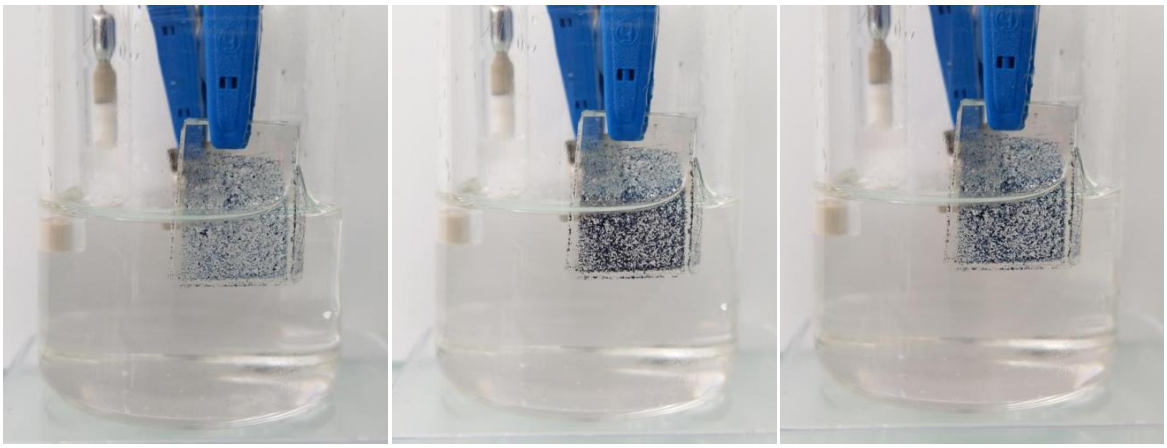

Figure 40: Spin coated $MoWO_x$ 1:1 film in the a) as-deposited, b) colored, c) bleached states after thermal treatment at 250°C for 1h.

While the spin coated $MoWO_x$ 1:1 obtained from non-heated precursor dispersions were the only films displaying an electrochromic activity for this deposition method, bar casting of $MoWO_x$ 2:1 NCs has led to films exhibiting reversible coloration/bleaching modulation. In the meantime, films made of MoO_{3-x} NCs could be colored from as deposited state into dark grey-blue, but could not be bleached back upon re-oxidation, therefore confirming the poor capacitive properties upon cycling previously observed in the CV analysis.

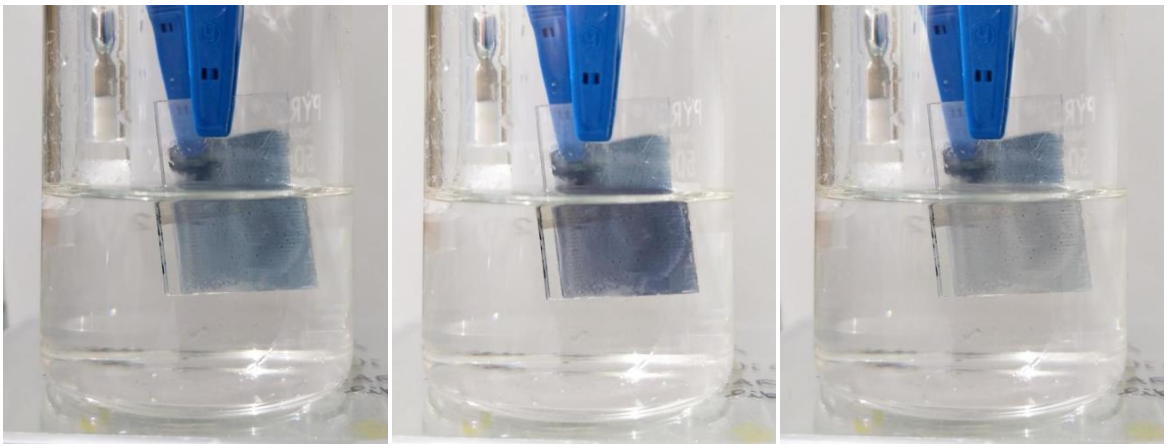

Figure 41: Bar coated $MoWO_x$ 2:1 film in the a) as-deposited, b) colored, c) bleached states.

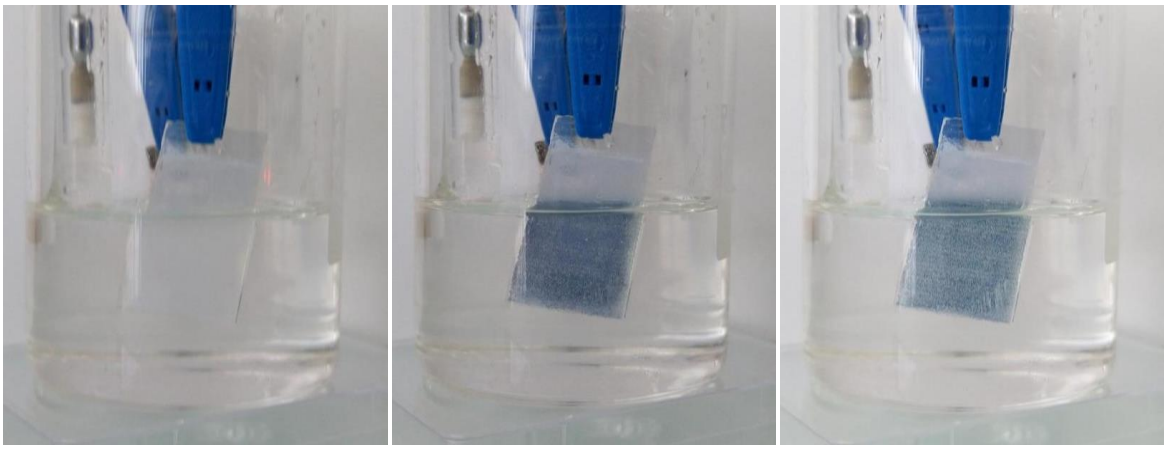

Figure 42: Spin coated MoO_{3-x} film in the a) as-deposited, b) colored, c) bleached states.

The improvement in electrochromic properties observed in the blade coated films might arise from the improved coverage and uniformity of the electrochromic material on the substrate, as observed visually and in the SEM images presented above (cf. *Figure 35*). This continuous layer combined with the uniformity and strong mechanical adherence provided by bar coating clearly impacts the electrochemical properties of the film in a significant way.

4.5. Conclusions

As a general result, all the bar-coated films could be visually colored and bleached with varying reversibility and durability abilities. On the other hand, the spin coated sample seems conceptually cyclable but suffers from poor contrast and film morphology. Given these observations, the blade coated $MoWO_x$ 2:1 is the best sample produced in the framework of this study, exhibiting a good contrast between states, a uniform film and reasonable electrochemical properties that can be trustfully compared with the WO_3 SMARTSPRAY reference in terms of contrast and reversibility (being of course far superior for now). Given these films are still in early testing and development phases, they are promising for future improvement and development of efficient electrochromic layers and devices.

We are well aware that the preliminary results presented in this section are mainly qualitative observations. Additional spectral measurements are necessary to complete these observations such as quantification of the optical contrast and spectral behavior of the films as a function of the applied potential to assess the NIR-selectivity of the material, arising from the LSPR it should support. These analyses are being carried out at ICMCB – University of Bordeaux while we write these lines.

Nevertheless, we managed to produce “proof-of-concept” electrochromically-active films using $MoWO_x$ dispersions deposited by both spin coating and bar casting. The formulation of the “electrochromic inks” and the parameters of deposition should be optimized in further research to improve the quality of the films and their electrochromic properties. Bar casting seems to be a very promising route for the deposition of efficient active layers. However, spin coating of the stabilized-suspensions also showed encouraging results in view of exploiting smaller volumes and material quantities for the deposition of electrochromic films.

Chapter 5 – Conclusions and perspectives

In this work, we studied the solvothermal synthesis of vacancy-doped molybdenum tungsten hybrid oxide, the behavior of the synthesized powders in suspension and their deposition as plasmonic electrochromic active films using wet deposition methods.

Using a simple, one step solvothermal synthesis, we produced several vacancy-doped oxides (namely $MoWO_x$ hybrids in molar ratios Mo/W = 1/1, 1/2 and 2/1, as well as MoO_{3-x} and WO_{3-x}). The powders recovered from the synthesis process were characterized. Microscopy imagery (TEM and SEM) confirmed the nanorod-shaped morphology of the hybrids while MoO_{3-x} and WO_{3-x} formed micrometric pellets and hexagonal particles respectively. These observation were supported by XRD measurements, with the hybrid nanorods probably formed from the insertion of Mo ions into the WO_3 crystal lattice base, with a preferential growth along the (002) plane of WO_3. Reflectance measurements of the powders exhibited the same tendencies as reported in the reference work of Yamashita et al., namely a 10+ fold increase in the absorbance of the hybrids compared to the pure oxides. We also studied the behavior of the powders when submitted to a thermal treatment. The results showed that both crystallinity and optical properties are well conserved after 1h of annealing up to 200°C in air and 500°C in Ar. The optical spectra also show a decrease in signal as the temperature of the treatment. This is in good accordance with the expected plasmonic nature of $MoWO_x$ compounds: as the temperature increases, the material is strongly oxidized, which induces the decreasing of the free charge carriers concentration and the intensity of the LSPR signal.

Then, the powders were dispersed in usual low toxic solvents (ethanol and water) to be used in the ensuing wet deposition methods. The suspensions were evaluated for their stability by the mean of qualitative visual observations and quantitative measurements of the zeta potential. The stability of raw suspensions (dispersant-free) in concentrations ranging from 0.5 to 10 mg/mL was very poor, holding for only a few minutes before heavy precipitation was observed. The stability could be improved using heavily loaded suspensions of 150 mg/ml, however, such concentrations are incompatible with most of the wet deposition methods considered here such as spray coating or spin coating in the case of very viscous suspensions. Therefore, the addition of dispersing agents was considered,, choosing them on the basis of the observations made in Chapter 1. This means that they should be compatible with the electrochromic application and could be eliminated using a moderate thermal treatment (<200°C) it they were shown to have a detrimental effect on the electrochromic properties of the deposited film. The best results were obtained for PEG 140k 20%wt. in ethanol and PEI 5%wt. in water at alkali pH. However, the elimination of PEI (250°C) requires temperature at which the properties of the active material starts to degrade, thus PEI was ruled out. As a consequence, only PEG 140k was selected as a stabilizing agent for preparing EtOH-based inks. Noteworthily, the use of polyethyleneoxide-based agents can be of later benefit on the electrochromic properties of the active material thanks to their affinity for Li^+ ions.

10 mg/mL suspensions with PEG in ethanol and 150 mg/ml surfactant-free suspensions in ethanol were used for spin coating and bar casting respectively. Because of time considerations, only representative cases were studied, namely $MoWO_x$ 1:1 for spin coating and MoO_{3-x} and $MoWO_x$ 2:1 in the case of bar casting. In addition, previously reported highly efficient electrochromic WO_3 SMARTSPRAY reference films were used as a reference for comparison of the performances of our plasmonic films. All films presented here displayed an observable modulation of visible light while the reversibility of the process varied from one case to the other. The WO_3 SMARTSPRAY film could exhibit great coloration, reversibility and durability as it could be expected. The spin coated $MoWO_x$ 1:1 showed electrochromic functionality but displayed poor irreversible contrast between the colored and bleached states in addition to inhomogeneous film morphology. Similarly, the blade coated MoO_{3-x} could be colored but would not bleach, confirming the poor reversibility observed in the CV curves of the film. In comparison, the bar casted $MoWO_x$ 2:1 was the best film obtained by ending this work. The deposited film is homogeneous, displays a good visual contrast between states, as well as reasonable reversibility and durability through cycling.

In conclusion, even though the plasmonic nature and corresponding NIR-selective modulation properties of molybdenum tungsten hybrid oxide could not be highlighted in the frame of this work, we still managed to deposit several electrochromically-active proof-of-concept films using $MoWO_x$ NCs dispersions in low toxic media and two wet coating methods: spin coating and bar casting.

In terms of perspective, the first priority would be to obtain more information towards the confirmation of the plasmonic behavior of the hybrid materials. Therefore, further research should be conducted in this direction. Some of these measurements are already in progress or planned for a very near future, more precisely X-ray photoelectron spectroscopy (XPS) and electron paramagnetic resonance (EPR) performed at ICMCB – University of Bordeaux (A. Rougier). These complementary analyses will allow the in-depth study of the stoichiometry of the hybrid materials at different Mo/W ratios, including their concentration in oxygen vacancies and the verification of its sufficiency to support LSPR properties. Another useful analysis technique in the context is the scanning transmission electron microscopy coupled with electron energy loss spectroscopy (STEM-EELS). Mapping of the particles using this method can highlight the presence of plasmonic signature in a material and their location on the actual particle (bulk, surface, edges, corners…). The latter is made possible by the current collaboration between GREENMAT and U. Paris-Sud (Dr. M. Kociak), samples have already been sent for analysis and the results should be recovered in the near future.

Also, the powders and their synthesis should be further studied. For example, the monitoring of the synthesis during the solvothermal process could be studied. To this purpose, an advanced equipment allowing sampling during the synthesis, available by GREENMAT, could be exploited in future research. In-depth study of the properties of the powders could be considered, with additional information gather from methods such as Rietveld measurements to better understand the crystallinity of the hybrids and therefore their formation process. New intermediate Mo/W ratios and their effect on the properties of the material could also be part of future studies. Most of all, reflectance measurements of the powders should be further studied to develop and reliable and controlled measurement protocol using the equipment available at the GREENMAT.

In addition, theoretical simulations could be performed benefitting from the collaboration with UNamur (L. Henrard) to better understand and anticipate the impact of different parameters on the overall properties of the powder. These calculations are also planned for a near future.

The dispersion of the powders to formulate better and more stable suspensions is of major importance since the electrochromic properties of the film could depend on the quality of the deposition. If sufficient stability is reached, deposition using other deposition methods such as spray coating techniques could be carried, ultimately targeting films of improved efficiency and long term durability (tested over 500+ charging cycles) that could be implemented in a complete device.

Finally, large-scale devices could be used as a new generation of selective “smart windows” in energy-efficient buildings if their electrochromic properties and durability in lab-scale and real-life conditions meet the requirements of such devices.

References

1. Cao, X. et al. “Building energy-consumption status worldwide and the state-of-the-art technologies for zero-energy buildings during the past decade” *Energy Build.* **2016**, *128*, 198–213.
2. Policy Pathways: Modernising Building Energy Codes, OECD/IEA- International Energy Agency, UNDP- United Nation Development Programme, USA, edition 2013.
3. Wang, Y. et al. “Switchable Materials for Smart Windows” *Annu. Rev. Chem. Biomol. Eng* **2016**, *7*, 283–304.
4. Karami, Peyman. (2015). Robust and Durable Vacuum Insulation Technology for Buildings.
5. https://epthinktank.eu/2016/07/08/energy-efficiency-in-buildings/energy-consuption-by-sector/, consulted on the 11th of June
6. Niachou, A. et al. “Analysis of the green roof thermal properties and investigation of its energy performance” *Energy Build.* **2001**, *33* (7), 719–729.
7. Austin, R. R. Solar control properties in low emissivity coatings. U.S. Patent 5183700A, August 10, 1990.
8. https://www.greenmatch.co.uk/double-glazing/double-glazed-windows, consulted on the 16th of June
9. https://oknalux.com.au/importance-of-low-e-glass/, consulted on the 16th of June
10. http://www.verre-solutions.com/content/verre-electrochrome, consulted on the 16th of June
11. Denayer, J. et al. “Improved coloration contrast and electrochromic efficiency of tungsten oxide films thanks to a surfactant-assisted ultrasonic spray pyrolysis process” *Sol. Energy Mater. Sol. Cells* **2014**, *130*, 623–628.
12. Mortimer, R. J. “Electrochromic Materials” *Annu. Rev. Mater. Res.* **2011**, *41*, 241–268.
13. Chatzikyriakou, D. et al. “Mesoporous amorphous tungsten oxide electrochromic films: a Raman analysis of their good switching behavior” *Microporous Mesoporous Mater.* **2017**, *240*, 31–38.
14. Denayer, J. et al. “Surfactant-assisted ultrasonic spray pyrolysis of nickel oxide and lithium-doped nickel oxide thin films, toward electrochromic applications” *Appl. Surf. Sci.* **2014**, *321*, 61–69.
15. Moulki, H. et al. “Improved electrochromic performances of NiO based thin films by lithium addition: From single layers to devices” *Electrochim. Acta* **2012**, *74*, 46–52.
16. Runnerstrom, E. L. et al. “Nanostructured electrochromic smart windows: traditional materials and NIR-selective plasmonic nanocrystals” *Chem. Commun* **2014**, *50*, 10555.
17. Dasgupta, B. et al. “Detrimental Effects of Oxygen Vacancies in Electrochromic Molybdenum Oxide” *J. Phys. Chem. C* **2015**, *119*, 10592–10601.
18. Mortimer, R. J. et al. ”Electrochromic organic and polymeric materials for display applications” *Displays* **2006**, *27*, 2–18.
19. Ma, C. et al. *Smart Sunglasses and Goggles Based on Electrochromic Polymers*.
20. Sauvet, K. et al. “IR electrochromic WO3 thin films: From optimization to devices” *Sol. Energy Mater. Sol. Cells* **2009**, *93* (12), 2045–2049.
21. Santos, L. et al. ”Structure and Morphologic Infl uence of WO 3 Nanoparticles on the Electrochromic Performance of Dual-Phase a -WO 3 / WO 3 Inkjet Printed Films” *Adv. Electron. Mater.* **2015**, 1–10.
22. Hepel, M. et al. ”Electrochromic WO3−x films with reduced lattice deformation stress and fast response time” *Electrochim. Acta* **2007**, *52* (11), 3541–3549.
23. Li, H. et al. “Spray coated ultrathin films from aqueous tungsten molybdenum oxide nanoparticle ink for high contrast electrochromic applications” *J. Mater. Chem. C* **2015**, *4*, 33–38.
24. Agrawal, A. et al. “Localized Surface Plasmon Resonance in Semiconductor Nanocrystals” *Chem. Rev.* **2018**, *118*, 3121–3207.
25. Yin, H. et al. “Localized Surface Plasmon Resonances in Plasmonic Molybdenum Tungsten Oxide Hybrid for Visible-Light-Enhanced Catalytic Reaction” *J. Phys. Chem. C* **2017**, *121*, 23531–23540.
26. Llordes, A. et al. In *Electrochromic Materials and Devices*: Weinheim, Germany, 2015; pp 363–398.
27. Rycenga, M. et al. “Controlling the Synthesis and Assembly of Silver Nanostructures for Plasmonic Applications” *Chem. Rev.* **2011**, 111, 3669−3712.
28. Mulvihill, M. J. et al. ”Anisotropic Etching of Silver Nanoparticles for Plasmonic Structures Capable of Single-Particle SERS” *J. Am. Chem. Soc.* **2010**, 132, 268−274.
29. Gansel, J. K. et al. ”Gold Helix Photonic Metamaterial as Broadband Circular Polarizer” *Science* **2009**.
30. Pors, A. et al. “Plasmonic Nanoantennas to Split-Ring Resonators: Tuning Scattering Strength” *J. Opt. Soc. Am. B* **2010**, 27, 1680−1687.
31. Garcia, G. et al. “Dynamically modulating the surface plasmon resonance of doped semiconductor nanocrystals” *Nano Lett.* **2011,** 11, 4415–4420.
32. Brousse, T. et al. “To Be or Not To Be Pseudocapacitive?” *J. Electrochem. Soc.* **2015**, *162* (5), 5185–5189.

33. Henglein, A. et al. "Chemistry of Agn aggregates in aqueous solution: non- metallic oligomeric clusters and metallic particles" *Faraday Discuss*. **1991**, 92, 31–44.
34. Ung, T. et al. "Spectroelectrochemistry of colloidal silver" *Langmuir* **1997**, 13, 1773–1782.
35. Boschloo, G. et al. "Spectroelectrochemistry of highly doped nanostructured tin dioxide electrodes" *J. Phys. Chem. B* **1999,** 103, 3093–3098.
36. Wang, C. et al. "Electrochromic nanocrystal quantum dots" *Science* **2001**, 291, 2390–2392.
37. Novo, C. et al. "Electrochemical charging of single gold nanorods" *J. Am. Chem. Soc.* **2009**, 131, 14664–14666
38. Coughlan, C. et al. "Compound Copper Chalcogenide Nanocrystals" *Chem. Rev.* **2017**, 117, 5865−6109.
39. S. D. Lounis, E. et al. "Defect chemistry and Plasmon physics of colloidal metal oxide Nanocrystals," *J. Phys. Chem. Lett.* **2014**, 5, 1564–1574.
40. Kim, J. et al. "Nanocomposite Architecture for Rapid, Spectrally-Selective Electrochromic Modulation of Solar Transmittance" *Nano Lett* **2015**, *15*, 5574–5579.
41. Manthiram, K. et al. "Tunable Localized Surface Plasmon Resonances in Tungsten Oxide Nanocrystals" *J. Am. Chem. Soc* **2012**, *134*, 3998.
42. Maho, A. "Single material dual-band electrochromic based on sprayed plasmonic tungsten oxide" unpublished work
43. https://www.energy.gov/sites/prod/files/2015/05/f22/emt97_Garcia_041515.pdf, consulted on the 14th of June
44. Spetter, D. et al. "Solvothermal Synthesis of Molybdenum−Tungsten Oxides and Their Application for Photoelectrochemical Water Splitting" *ACS Sustain. Chem. Eng* **2018**, *6*, 12641–12649.
45. Wang, X. D. et al. "Novel porous molybdenum tungsten phosphide hybrid nanosheets on carbon cloth for efficient hydrogen evolution" *Energy Environ. Sci.* **2016**, *9* (4), 1468–1475.
46. Yin, H. et al. "Plasmonic metal/Mo x W 1Àx O 3Ày for visible-light-enhanced H 2 production from ammonia borane" *J. Mater. Chem. A* **2018**, *6*, 10932–10938.
47. Cheng, H. et al. "Harnessing single-active plasmonic nanostructures for enhanced photocatalysis under visible light" *J. Mater. Chem. A* **2015**, *3* (10), 5244–5258.
48. Zhou, H. et al. "Molybdenum−Tungsten Mixed Oxide Deposited into Titanium Dioxide Nanotube Arrays for Ultrahigh Rate Supercapacitors" *Appl. Mater. Interfaces* **2017**, *9*, 18669–18709.
49. Li, H. et al. "Nanohybridization of molybdenum oxide with tungsten molybdenum oxide nanowires for solution-processed fully reversible switching of energy storing smart windows" *Nano Energy* **2018**.
50. Li, H. et al. "Solution-Processed Porous Tungsten Molybdenum Oxide Electrodes for Energy Storage Smart Windows" *Adv. Mater. Technol.* **2017**, *2* (8), 1700047.
51. Gesheva, K. A. et al. "Crystallization of chemically vapor deposited molybdenum and mixed tungsten/molybdenum oxide films for electrochromic application" *Thin Solid Films* **2007**, *515*, 4609–4613.
52. Zaleska-Medynska, A. et al. *Metal oxide photocatalysts*; Elsevier, 2018.
53. https://www.researchgate.net/figure/Schematic-diagram-of-the-autoclave-used-in-solvothermal-hydrothermal-synthesis-23_fig4_265051178, consulted on the 17th of June
54. Arfken, G. B. et al. *Probability and Statistics*; Academic Press, 2013.
55. Dhandayuthapani, T. et al. "High coloration efficiency, high reversibility and fast switching response of nebulized spray deposited anatase TiO2 thin films for electrochromic applications" *Electrochim. Acta* **2017**, *255*, 358–368.
56. Lee, S.-H. et al. "Crystalline WO3 Nanoparticles for Highly Improved Electrochromic Applications" *Adv. Mater.* **2006**, *18* (6), 763–766.
57. Maho, A. "ITO solvothermal", publication just accepted.
58. Bertus, L. M. et al. "Prediction of TiO_2 and WO_3 Nanopowders Surface Charge by the Evaluation of Point Of Zero Charge (PZC)" *Environ. Eng. Manag. J.* **2011**, *10* (8), 1021–1026.
59. A.-S. Duwez, *Cours de Surafces et interfaces*. ULiège.
60. Peng, C. et al. "Enhancing the Layer-by-Layer Assembly of Indium Tin Oxide Thin Films by Using Polyethyleneimine," *J. Phys. Chem. C* **2010**, 114, 9685–9692.
61. Borodko, Y. et al. "Probing the interaction of poly(vinylpyrrolidone) with platinum nanocrystals by UV-Raman and FTIR," *J. Phys. Chem. B* **2006**, 110, 23052–23059.
62. Said, Z. et al. "Performance enhancement of a Flat Plate Solar collector using Titanium dioxide nanofluid and Polyethylene Glycol dispersant" *J. Clean. Prod.* **2015**, *92*, 343–353.
63. Scriven, L. E. "Physics and Applications of DIP Coating and Spin Coating" *MRS Proc.* **1988**, *121*, 717.
64. Berni, A.; Mennig, M.; Schmidt, H. *2.2.8 DOCTOR BLADE*.
65. Runnerstrom, E. L.; Lars, E. Charge transport in metal oxide nanocrystal-based materials, 2016.

Annexes

I. Characterization methods

a) TEM

Transmission electronic microscopy (TEM) is an imagery technique that allows the observation of particles at high magnification for determination of their morphology and size. The acquisition of the micrographs is based on the transmission of an electron beam through a thin sample. As the thickness and density of the material increase, fewer electrons reach the detector below. This creates a contrast between the regions of high and low coverage densities, creating a monochromic picture of the sample.

For the preparation of the samples, a drop of a low boiling point solvent (ethanol for example) containing the compound of interest is placed on a copper grid and evaporated. Thanks to this process, solid particles can be deposited as a monolayer if the concentration is low enough, enabling the observation of individual particles. Sometimes, one side of the grid is covered with a carbon film to allow the deposition of small particles that would pass through the mesh because of their small size.

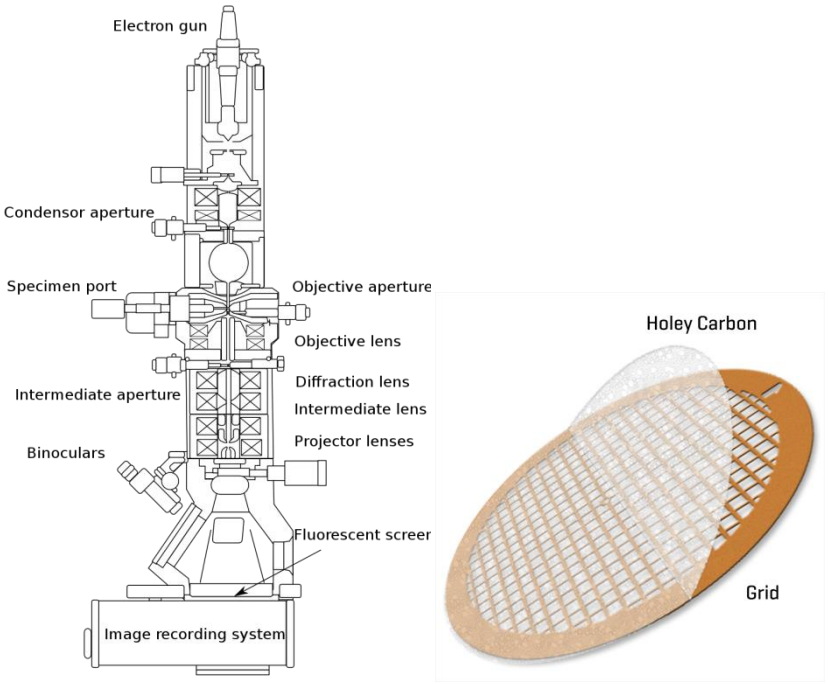

Figure A1: Schematic representation of the TEM equipment (right)[1] and the copper grid (left)[2].

b) SEM and EDX

Scanning electron microscopy (SEM) is related to the TEM imagery technique to the extent that both allow the characterization and measurement of the morphological properties of a material such as size and shape. However, the principles by which the micrographs are acquired differ significantly.

In SEM, an electronic beam is focused on the sample. If the sample is not intrinsically conductive, the surface can be covered with a layer of a highly conductive material such as Au, Ag, C or Pt. The interaction between the electron beam and the conductive material leads to the emission of secondary electron of lower energy. The detection of these secondary electrons defines a representation of the surface and the topography of the sample.

In addition, the nature of the materials can be studied using the same instrument. Indeed, the interaction between the electron beam and matter can give place to many different signals all bearing information about the sample. Energy dispersive X-ray (EDX) measurement allows the characterization of the material at an elemental level. If the incident electron beam interacts with electrons in the inner electronic shells and transfers its energy, the electron can either "jump" to a higher energy level or can be ejected from the atom. In both case, the displacement of the electron leaves a hole in the low energy shells. An electron from an outer shell will therefore fill this hole. The difference in energy between the two levels can be emitted in the form of X-rays. Each element presents a characteristic EDX signature composed of different rays acting as a "fingerprint" that can be easily spotted in the EDX spectrum of the material. This technique therefore allows the semi-quantification of the species present in a sample.

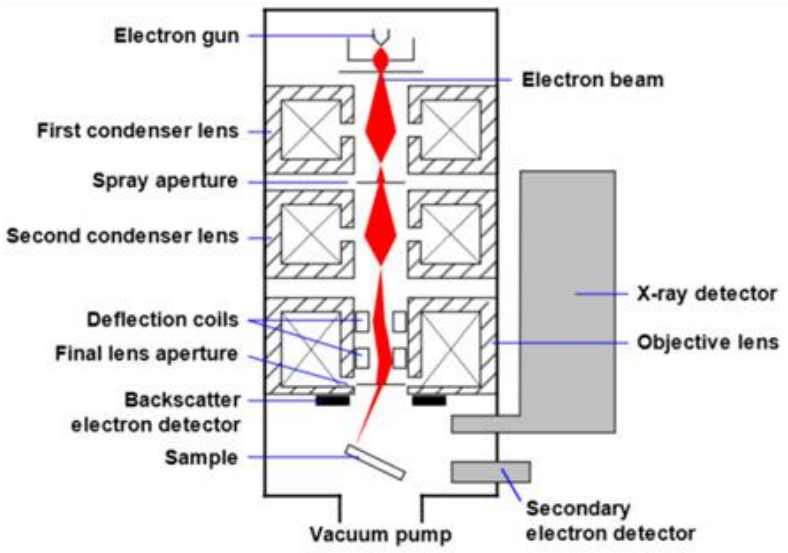

Figure 2A: Schematic representation of the SEM equipment[3].

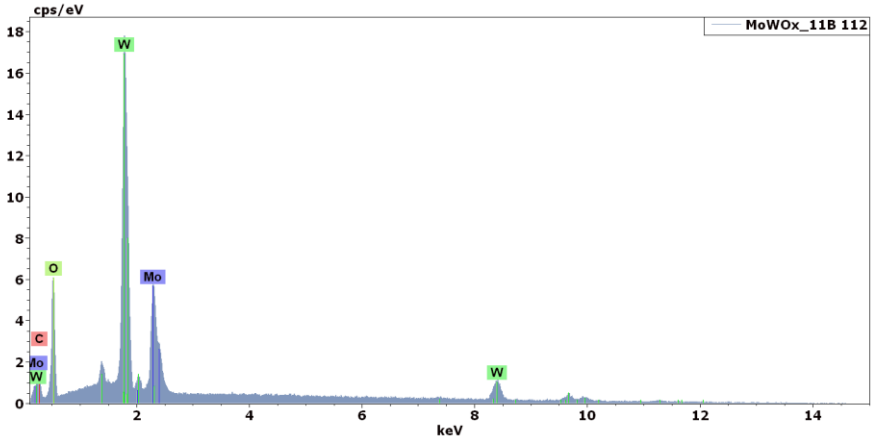

Figure 3A: Example of an EDX spectrum of the $MoWO_x$ 1:1 powder.

c) <u>XRD</u>

Information about the crystallinity and the different phases in a given material can be recovered from the characterization of a sample by X-ray diffraction.

When X-rays interact with crystalline substances, they are diffracted by the atoms of the lattice, inducing interferences between the beams. These interference can be constructive if they satisfy Bragg's law, defined as:

$$2d \sin\theta = n\lambda$$

With d the reticular distance, θ the scattering angle, λ the wavelength of the incident X-ray beam and n a positive integer.

Depending on the angle of the incident beam and the distance between the atoms forming the lattice of the material, both destructive and constructive interference can take place (as shown in Figure X). In the case of a constructive interference, the signal will lead to a set of characteristic diffraction rays that can be identified in the diffractogram of the sample.

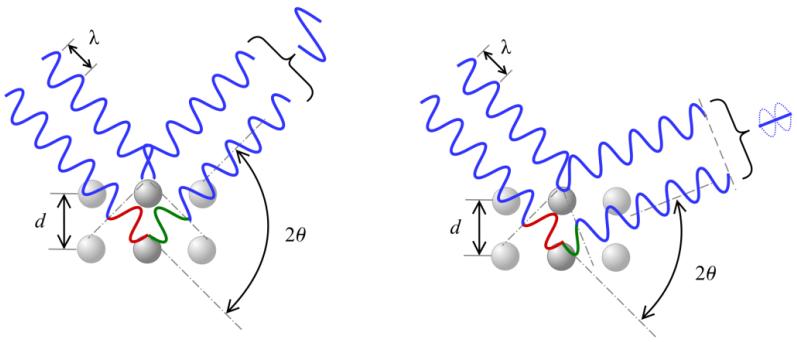

Figure 4A: Representation of the interference phenomenon arising from the diffraction of X-rays in crystals[4].

d) Zeta potential

The zeta potential describes the charge appearing at the interface between the surface of a particle and a liquid. The charges at the surface of the particles interact with the ions in the liquid, modifying their distribution in the media. This phenomenon causes the formation of a double charge layer at the interface.

The first charge layer is well organized and consists in ions tightly bound to the surface of the particles thanks to the attraction between opposite charges. The second layer, farther from the interface, is also called the diffuse layer. In this region, ions are not bound anymore and the potential decreases as a function of the distance to the interface. This effect is due to the increasing role of the random thermal agitation of the ions as the potential gradually decreases. Since the zeta potential can be linked to the charge at the surface of the particles, and therefore to the electrostatic repulsion between the latter, this measurement can be used as an indicator of the colloidal stability of the particles in suspension.

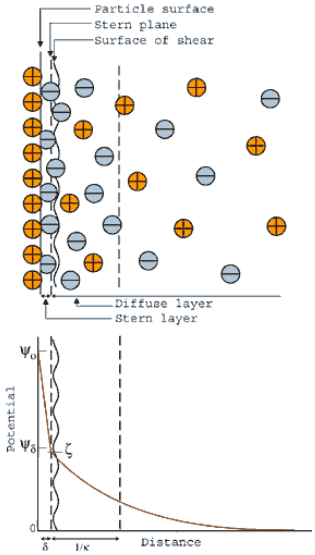

Figure 5A: Representation of the double-layered organization of the charges in the vicinity of a particle in suspension[5].

The zeta potential can be measured using an electroacoustic phenomenon known as the colloid vibration current. When an ultrasound wave propagates through a liquid media, the particles and ions in this media are displaced at different rates, thus disturbing the double layer structure around the particles. The fluid flow caused by the wave drags the ions of the double layer towards one of the poles of the particle. This displacement of charges induces an excess of charges at one of the poles and a corresponding excess of opposite charges at the other pole. This charge gradient in the vicinity of the particle induces a dipole moment in the latter, generating an electric field in the liquid. By measuring the electric current arising from the induced electric field, and knowing the size of the particles, their density and the weight content of the suspension, it is possible to determine the zeta potential per particle of the suspended material.

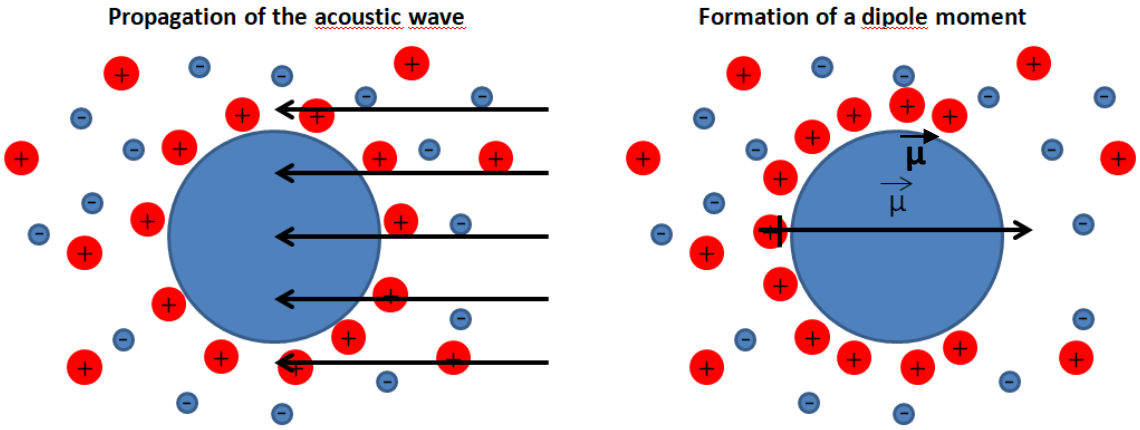

Figure 6A: Electroacoustic measurement of the surface potential of a particle in suspension.

e) *UV-Vis-NIR spectrophotometry*

In spectrophotomerty, an incident radiation is sent on a sample (suspension, thin film…). Interactions between the optically active species and the incident light wave can give rise to absorbance, emission or scattering from the electronic transition taking place in the active molecules. The measurement of the resulting spectrum highlights the wavelength at which these phenomena take place.

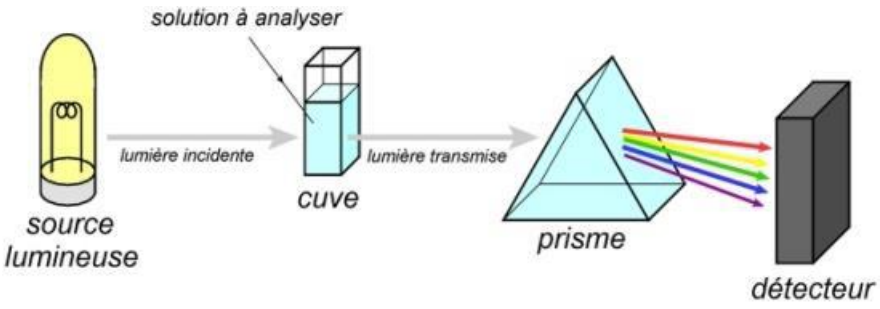

Figure 7A: Schematic representation of the measurement using a spectrophotometer equipment[5].

For diffuse reflectance measurements of powders, the sample needs to be placed in an integrating sphere (*Figure 8A*). If the incident radiation is reflected more than once by the powder, it is said to be diffuse reflected light (in comparison with specular reflected light which is only reflected once) (*Figure 8A*)

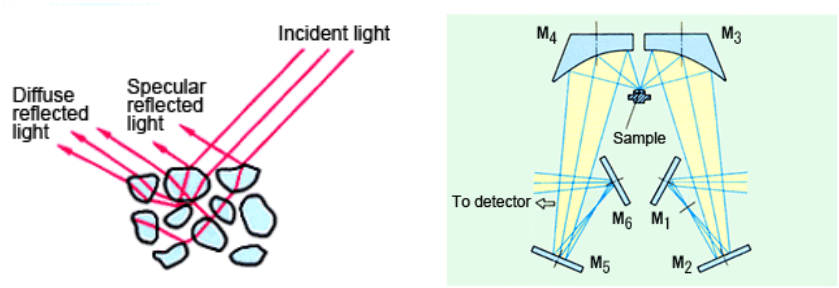

Figure 8A: Representation of the specular and diffuse reflectance in a powder (left) and schematic representation of a integrating sphere set-up (right)[6].

f) Electrochemical techniques: CV & potentiostatic / CA

Cyclic Voltammetry (CV) measurements imply the application of a triangular application: a potential ramp is applied at a constant rate, followed by the inverted scan going back to the starting potential.

In a fully reversible system, the CV curves exhibit a "duck" shape, with the oxidation peak and the reduction peak present in similar intensities on the forward and backward scans respectively in the example below. This characteristic shape shows that all the oxidized/reduced species are reduced/oxidized back to their original state during the inverted scan (with the condition that the scanning rate should be faster than the reaction rate for the chemical transformation of the species in the potential interval).

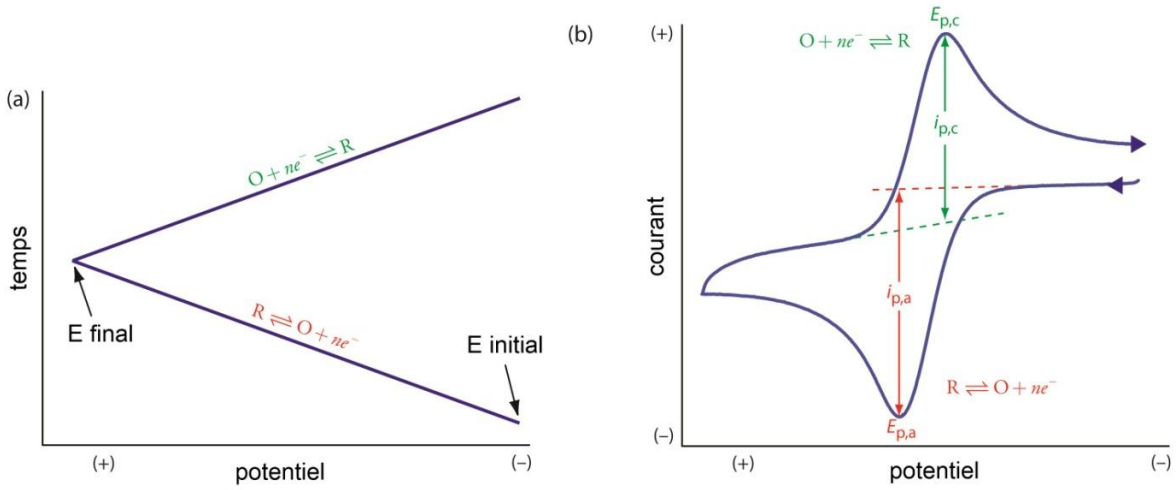

Figure 10A. Triangular variation of the potential as a function of time (a), typical CV curve of a reversible sample (b)[7].

Chronoamperometry measurements (CA) imply the application of a stepped potential at the working electrode. The resulting current, arising from the faradaic phenomenon taking place at the electrode after the application of the potential step, is monitored as a function of time. The relationship between the electrical signal and time can be established after a single or multiple potential steps.

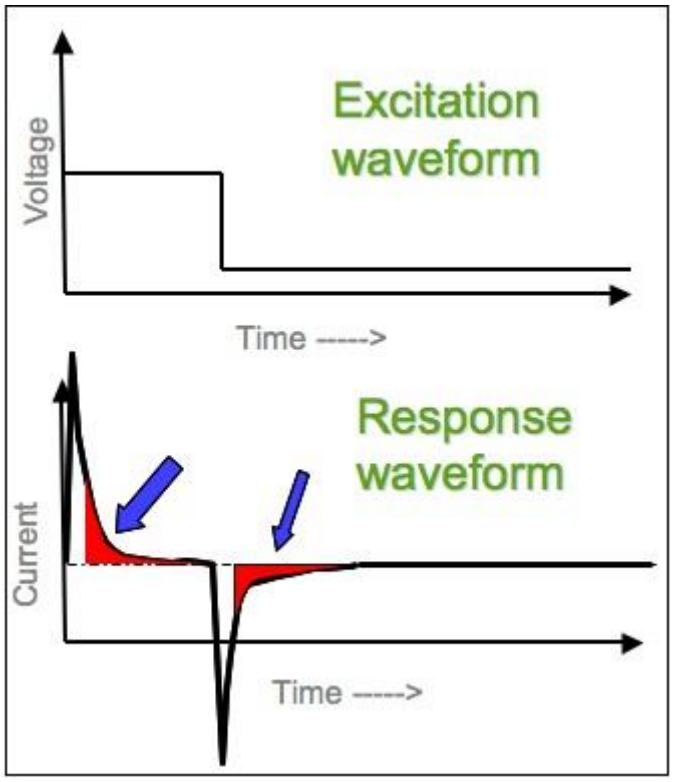

Figure 11A: Representation of the stepped bias (top) and the resulting current response (bottom)[7].

Annexes references:

1. https://fr.wikipedia.org/wiki/Microscopie_%C3%A9lectronique_en_transmission, consulted on the 05/06

2. https://emresolutions.com/product/lacey-carbon-film-on-copper-200-mesh-50/, consulted on the 07/06

3. https://www.nanoscience.com/techniques/scanning-electron-microscopy/, consulted on the 05/06

4. https://en.wikipedia.org/wiki/Bragg%27s_law#/media/File:Braggs_Law.svg, consulted on the 06/06

5. https://www.brookhaveninstruments.com/what-is-zeta-potential, consulted on the 06/06

6. Laura Comeron, Master Thesis, ULiège, 2016

7. Anthony Maho, Thesis, UNamur, 2014